https://doi.org/10.5194/tc-2021-391
Preprint. Discussion started: 23 December 2021

The Cryosphere Discussions
Open Access

Wave-triggered breakup in the marginal ice zone generates lognormal floe size distributions

Nicolas Mokus[1] and Fabien Montiel[1]

[1]Department of mathematics and Statistics, University of Otago, Dunedin, New Zealand

Correspondence: Nicolas Mokus (nmokus@maths.otago.ac.nz)

Abstract. Fragmentation of the sea ice cover by ocean waves is an important mechanism impacting ice evolution. Fractured ice is more sensitive to melt, leading to a local reduction in ice concentration, facilitating wave propagation. A positive feedback loop, accelerating sea ice retreat, is then introduced. Despite recent efforts to incorporate this process and the resulting floe size distribution (FSD) into the sea ice components of global climate models (GCM), the physics governing ice breakup under wave action remains poorly understood, and its parametrisation highly simplified. We propose a two-dimensional numerical model of wave-induced sea ice breakup to estimate the FSD resulting from repeated fracture events. This model, based on linear water wave theory and viscoelastic sea ice rheology, solves for the scattering of an incoming time-harmonic wave by the ice cover and derives the corresponding strain field. Fracture occurs when the strain exceeds an empirical threshold. The geometry is then updated for the next iteration of the breakup procedure. The resulting FSD is analysed for both monochromatic and polychromatic forcings. For the latter results, FSDs obtained for discrete frequencies are combined appropriately following a prescribed wave spectrum. We find that under realistic wave forcing, lognormal FSDs emerge consistently in a large variety of model configurations. Care is taken to evaluate the statistical significance of this finding. This result contrasts with the power-law FSD behaviour often assumed by modellers. We discuss the properties of these modelled distributions, with respect to the ice rheological properties and the forcing waves. The projected output will be used to improve empirical parametrisations used to couple sea ice and ocean waves GCM components.

1 Introduction

Sea ice is a distinctive feature of both polar oceans and has a profound influence on our climate. It blankets a significant fraction of the Earth, is hard to reach, and offers particularly harsh fieldwork conditions. Consequently, numerical modelling is a valuable tool not only for forecasting ice extent evolution, but also to gain insights, at a global scale, into the physical processes shaping this evolution. Hindcasting results straying away from observations (Stroeve et al., 2007) hints at not fully understood internal climate variability (Zhang et al., 2018; Castruccio et al., 2019) or missing physics, such as the effect of waves on the ice cover (Squire, 2020). Global coupled models (GCM) have typically overlooked this impact, even if advances were made in recent years (Roach et al., 2018; Boutin et al., 2020a). Waves can break the ice, especially as thinner ice becomes prevalent. For instance, the 2012 record-low Arctic sea ice extent was amplified by wave activity (Parkinson and Comiso,

https://doi.org/10.5194/tc-2021-391
Preprint. Discussion started: 23 December 2021

2013). With thinner and weaker first-year ice becoming dominant (Kwok et al., 2009; Kwok, 2018), the sea ice grows more vulnerable to flexure-induced failure.

The marginal ice zone (hereafter MIZ), a belt of loosely to densely packed ice floes, serves as a buffer between the ice-free open ocean and the pack ice; it is a region notably affected by waves (Dumont et al., 2011). The individual description of these isolated, floating pieces of sea ice is not possible. Since the pioneering work of Rothrock and Thorndike (1984), researchers have taken interest in describing the floe size distribution (hereafter FSD) and its effect on the climate system. In particular, fragmentation caused by ocean waves makes the floes more sensitive to melt (Steele, 1992; Perovich and Jones, 2014), even for larger ones (Horvat et al., 2016), locally decreasing the ice concentration and allowing waves to propagate further into the MIZ. It leads to more fragmentation, thus introducing an ice–wave feedback loop (Asplin et al., 2012; Thomson and Rogers, 2014).

Remote sensing and airborne observations of floe sizes (e.g. Rothrock and Thorndike, 1984; Toyota et al., 2006; Steer et al., 2008; Toyota et al., 2011; Wang et al., 2016) have led to the rooted conception that the FSD follows a power law; an – often truncated – Pareto distribution. However, a variety of processes such as failure from wind or internal stress, lateral melting or growth, ridging, rafting or welding, are susceptible to alter the FSD. Hence, it is unclear how wave action may have been behind those findings, as wave conditions prior or during observations, as well as ice properties, are not always reported (Herman et al., 2021). Additionally, a broad spectrum of acquisition techniques, areas and times of studies, and a priori assumptions led to parametrisations of this power law covering a large span of exponents. Stern et al. (2018) exposed that the widespread distribution fitting technique used, least squares regressions in log-log space, is likely to have led to significant bias in these exponent estimates.

Although an extensive body of observational research (e.g. Squire and Moore, 1980; Wadhams et al., 1988; Meylan et al., 2014; Montiel et al., 2018) has been conducted on quantifying the attenuation of ocean waves within a field of ice floes, the reciprocal response of the ice to the waves is unsatisfactorily understood as direct observations of wave-induced floe breakup are scarce, and localised both in time and space. Various models have implemented a breakup parametrisation, either to investigate the FSD (Montiel and Squire, 2017; Herman, 2017) or to evaluate the impact of its introduction on other quantities such as ice thickness or concentration (Roach et al., 2018). These parametrisations are usually based on either stress (Williams et al., 2017; Montiel and Squire, 2017) or strain (Kohout and Meylan, 2008; Williams et al., 2013; Horvat and Tziperman, 2015; Boutin et al., 2018) or a combination of both (Dumont et al., 2011). When these quantities exceed a critical value, breakup is triggered. These models cover a large span of complexities, from ad-hoc configuration with simplified geometry to inclusion in a global sea ice model run in stand alone mode (Bennetts et al., 2017) or coupled to other GCM components (Roach et al., 2019; Boutin et al., 2020a). In this study, we model the wave-induced breakup process in isolation with the aim of quantifying the resulting FSD. We assume breakup happens on short time scales, as reported by Collins et al. (2015), allowing us to neglect other processes affecting the FSD.

A framework to model the evolution of the ice thickness distribution (ITD) has been introduced by Thorndike et al. (1975). The ITD does not have a preferred functional form (Dupont et al., 2021) and is usually represented at the sub-grid level in sea ice model, such as CICE (Hunke et al., 2021), by various thickness categories. Horvat and Tziperman (2015) extended this

https://doi.org/10.5194/tc-2021-391
Preprint. Discussion started: 23 December 2021

The Cryosphere Discussions

framework to include the floe size through a joint floe size and thickness distribution, which evolves under the action of separate physical processes such as thermodynamics, ridging and wave-induced breakup. Their formulation for the latter process relies on generating a unidirectional, random sea surface elevation transect (aimed at representing a GCM grid cell) from a prescribed spectrum. The elevation is then attenuated in the direction of propagation using an empirical fit to attenuation data generated by Kohout and Meylan (2008) that depends on ice thickness and wave period. Finally, the resulting strain is derived and used to parametrise the breakup. This scheme has then been implemented in CICE (Roach et al., 2018) to incorporate wave effects on the FSD, and, ultimately, sea ice dynamics and observable quantities such as ice concentration. Roach et al. (2019) further built upon this implementation by coupling CICE to a wave model, effectively delegating the wave attenuation previously handled within CICE.

Zhang et al. (2015) proposed a FSD theory treating breakup as a stochastic process redistributing floe sizes and abstracting the wave forcing into a model parameter, a so-called participation factor. The authors also included formulations for other FSD-rearranging processes, such as lead opening and ridging, but contrary to Horvat and Tziperman (2015) they make the FSD evolve alongside the ITD rather than considering the joint distribution. They extended their approach to an implementation in the sea ice model PIOMAS (Zhang et al., 2016), proposing a functional for the participation factor. They made it depend on the local wind, ice concentration, floe size and ice thickness. Hence, locally generated waves are taken into account, but the propagation and attenuation of swell waves are not included in a straightforward manner. The authors did not clarify the choice of this functional form, which depends on empirical parameters calibrated to replicate observations. This issue is dealt with assuming a power law distribution of floe sizes and the ensuing scale invariance property. Additionally, they fit power laws to their model results, without clarifying the fit method used nor the bias that may be introduced by binned data (Stern et al., 2018). In contrast, the approach used by Roach et al. (2018) allows for more flexibility as no parametric form is expected for the FSD. Nevertheless, the model sensitivity analysis conducted by Zhang et al. (2016) revealed compelling improvement on ice extent simulation when considering their FSD formulation.

Recent numerical experiments have been conducted to investigate the wave effect on the FSD without a priori assumptions on the distribution shape. Montiel and Squire (2017) extended the 3D linear wave scattering model of wave attenuation in the MIZ proposed by Montiel et al. (2016) by including a stress-based failure criterion. They investigated the FSD obtained after repeated breakup events and found that near normal or bimodal distributions emerged for a wide range of wave and ice conditions. However, computational constraints limited their ability to perform simulations on sufficiently large scales to conduct robust statistical analyses of these distributions. Herman (2017) coupled a non-hydrostatic, nonlinear wave model to sea ice represented as bonded grains, hence relaxing assumptions inherent to potential flow theory and allowing for the computation of a transient solution; at the expense of computational efficiency, limiting the usability of the model to smaller scale configurations. The resulting FSDs were narrow, bounded distributions governed by the grain sizes. Both approaches rely on some binning of the floe sizes, either directly (Montiel and Squire, 2017) or indirectly though the use of discrete elements (Herman, 2017), effectively ensuing discrete distributions. Recent observations of floes directly impacted by waves (Dumas-Lefebvre and Dumont, 2020; Herman et al., 2021) and laboratory experiments (Herman et al., 2018; Dolatshah et al., 2018; Passerotti et al., 2021) also suggest contrasting distributions. Despite indications that the power law FSD is not universally appropriate,

https://doi.org/10.5194/tc-2021-391
Preprint. Discussion started: 23 December 2021

The Cryosphere Discussions
Open Access
EGU

or linked to wave-induced breakup, wave modellers still use it to parametrise the MIZ in wave models (Williams et al., 2017; Boutin et al., 2020a, b).

We propose a model of wave–ice interaction, under monochromatic forcing, in an idealised domain. Our model takes wave scattering and dissipation into account and includes a strain-based breakup parametrisation. We let a FSD emerge by repeatedly breaking off floes from a semi-infinite ice cover, and we link the resulting distribution to the ice properties and the wave forcing. This approach is similar to the work presented by Montiel and Squire (2017); however, we simplify the geometry in order to generate sufficient breakup for robust statistical analysis. We observe that under a realistic wave forcing, our model generates FSDs appropriately described by lognormal distributions; this holds in a large span of model configurations. We discuss the effects of the wave and the ice properties on the distribution parameters. Even though we acknowledge that any parametric distribution is likely to be an inaccurate depiction of a real ice cover, they have the advantage of efficiently encoding the informations to be exchanged between GCM components (Horvat and Tziperman, 2015).

2 Preliminaries

We consider surface gravity waves propagating in a two-dimensional fluid domain of constant, finite depth H associated with a Cartesian coordinate system (x,z), where x and z are the horizontal and vertical coordinates, respectively. Translational invariance is assumed in the second horizontal direction. We assume the fluid to be inviscid and incompressible with density ρ_w. The flow is assumed to be irrotational so that the fluid velocity can be described by the gradient of a scalar potential Φ, which satisfies Laplace's equation:

$$\nabla^2\Phi = 0. \tag{1}$$

We place an array of $N_f + 1$ non-overlapping ice floes, modelled as floating visco-elastic plates, in the domain; two adjacent floes are separated by open-water. Their mechanical behaviour is determined by their density ρ, thickness h, flexural rigidity $D = \frac{Yh^3}{12(1-\nu^2)}$ (where Y and ν are respectively Young's modulus and Poisson's ratio), and viscosity γ; their draught is $d = \frac{\rho}{\rho_w}h$. Floe j, where $j \in \{0,\ldots,N_f\}$, is located in space by the horizontal coordinate of its left edge x_j (ordered so that $x_j < x_{j+1}$) and its length L_j, with L_{N_f} being infinite. At rest, the fluid region covered by floe j is encompassed in the sub-domain $\Omega^f_j = [x_j, x_j + L_j] \times [-H, -d]$. The interface with the ice $\partial\Omega^f_j$ is on $z = -d$. We denote $\Omega^f = \bigcup_0^{N_f} \Omega^f_j$ and $\partial\Omega^f = \bigcup_0^{N_f} \partial\Omega^f_j$. The ice-free sub-domain left of the floe-covered sub-domain Ω^f_j is Ω^w_j so that at rest,

$$\Omega^w_j = \begin{cases} [x_{j-1} + L_{j-1}, x_j] \times [-H, 0], & j > 0 \\ (-\infty, x_0] \times [-H, 0], & j = 0 \end{cases}. \tag{2}$$

The horizontal bottom boundary $\partial\Omega_H$ is at $z = -H$ and the interface $\partial\Omega^w_j$ between the atmosphere and Ω^w_j is at $z = 0$ when the fluid is at rest. We define Ω^w and $\partial\Omega^w$ in the same way as Ω^f and $\partial\Omega^f$. The whole fluid domain is $\Omega = \Omega^w \cup \Omega^f$. Our notations and the geometry of the model are summarized on Fig. 1.

The system is forced by a monochromatic plane wave of angular frequency ω propagating in the positive x direction. The wave amplitude a is assumed to be small compared to the wavelength. The perturbed top boundary of the fluid is located at

https://doi.org/10.5194/tc-2021-391
Preprint. Discussion started: 23 December 2021

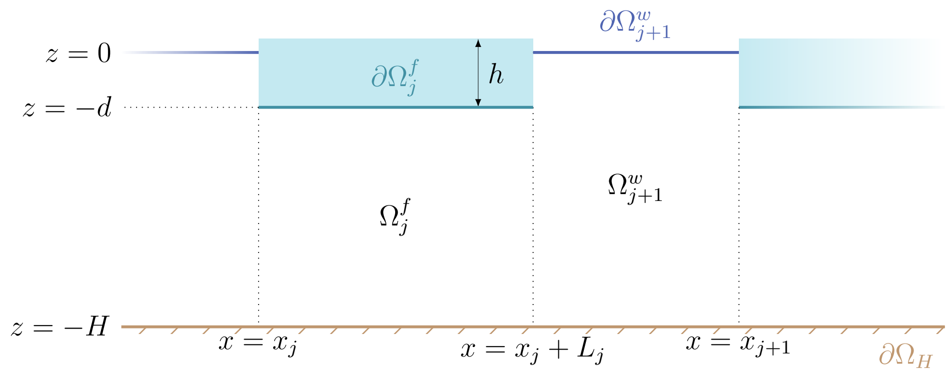

Figure 1. Geometry of the model at rest. Wave forcing would alter the fluid boundaries around $z=0$ and $z=-d$.

$z=\eta(x,t)$, whether it is an interface with the atmosphere (in which case $\eta\approx 0$) or with an ice floe (in which case $\eta\approx -d$). We further set $\Phi=\mathrm{Re}\left[\phi(x,z)\exp(-i\omega t)\right]$ with ϕ a time-independent, complex-valued function.

We consider the seabed to be impervious, hence not allowing for normal flow, so that on $\partial\Omega_H$

$$\frac{\partial\phi}{\partial z}=0. \tag{3}$$

The small amplitude forcing allows us to use linear surface waves theory in Ω^w, leading to the boundary condition

$$\frac{\partial\phi}{\partial z}=\frac{\omega^2}{g}\phi \tag{4}$$

on $\partial\Omega^w$, where g is the acceleration due to gravity. We model the flexural motion of the ice floes using the modified Kirchhoff-Love plate theory introduced by Robinson and Palmer (1990). Coupling to the fluid motion in Ω^f yields

$$\left(\frac{D}{\rho_w g}\frac{\partial^4}{\partial x^4}+1-\frac{\omega^2 d}{g}-i\frac{\gamma\omega}{\rho_w g}\right)\frac{\partial\phi}{\partial z}=\frac{\omega^2}{g}\phi \tag{5}$$

on $\partial\Omega^f$. Eqs. (4) and (5) stem from the assumptions that under small-amplitude wave forcing, waves do not break and fluid is at all time in contact with the bottom of the ice. Details on the derivations can be found in e.g. Fox and Squire (1994) or Williams et al. (2013).

We also neglect the surge motion of the floes, meaning that

$$\frac{\partial\phi}{\partial x}=0 \tag{6}$$

on $\{x_j,x_j+L_j\}\times[-d,0]$.

We finally add the free edge conditions

$$\frac{\partial^3\phi}{\partial x^2 z}=0,\quad \frac{\partial^4\phi}{\partial x^3 z}=0 \tag{7}$$

on $\{x_j,x_j+L_j\}\times\{-d\}$, which assume that bending moment and vertical stress vanish at the floe boundaries, respectively.

The boundary conditions given in Eqs. (3)-(7) together with Eq. (1) in its time-independent form, $\nabla^2\phi=0$, complete our boundary value problem.

https://doi.org/10.5194/tc-2021-391
Preprint. Discussion started: 23 December 2021

3 Methods

3.1 Wave scattering

In any sub-domain Ω_j^w or Ω_j^f, the velocity potential is decomposed as the superposition of a forward-travelling and a backward-travelling plane waves, using the ansatz $\left[c^+ e^{i\left(kx-\theta^+\right)} + c^- e^{-i\left(kx-\theta^-\right)}\right]\zeta(z)$, where $c^+, c^- \in \mathbb{C}$ are coefficients to be determined and $\theta^+, \theta^- \in [0, 2\pi)$ are phase shifts introduced to simplify analytical derivations and improve numerical stability. Solving the boundary value problem described in Sect. 2 in all sub-domains, the potential is expanded into series of wave modes

$$\phi = \begin{cases} \sum_{n=0}^{\infty} \left[c_{j-1,n}^{w+} e^{i\left(k_n^w x - \theta_{j-1,n}^{w+}\right)} + c_{j,n}^{w-} e^{-i\left(k_n^w x - \theta_{j,n}^{w-}\right)}\right]\zeta_n^w(z), & (x,z) \in \Omega_j^w \\ \sum_{n=-2}^{\infty} \left[c_{j,n}^{f+} e^{i\left(k_n^f x - \theta_{j,n}^{f+}\right)} + c_{j,n}^{f-} e^{-i\left(k_n^f x - \theta_{j,n}^{f-}\right)}\right]\zeta_n^f(z), & (x,z) \in \Omega_j^f \end{cases} \tag{8}$$

where superscripts w or f are related to an open-water or floe-covered sub-domain.

The wave numbers $\{k_n^w \mid n \geq 0\}$ are the roots of the dispersion relation

$$k \tanh(kH) = \frac{\omega^2}{g} \tag{9}$$

such that k_0^w is a positive real number (therefore associated with left- and right-propagating wave modes in Ω^w) while $\{k_n^w \mid n > 0\}$ are purely imaginary numbers with positive imaginary part, sorted by ascending imaginary part (associated with exponentially decaying evanescent wave modes).

Likewise, the wave numbers $\{k_n^f \mid n \geq -2\}$ are the roots of the dispersion relation

$$\left(\frac{D}{\rho_w g}k^4 + 1 - \frac{\omega^2 d}{g} - i\frac{\gamma\omega}{\rho_w g}\right) k \tanh(k(H-d)) = \frac{\omega^2}{g} \tag{10}$$

such that $\{k_n^f \mid n > -2\}$ are complex numbers in the first quadrant of the complex plane, sorted by ascending imaginary part for $n > 0$, and k_{-2}^f is a complex number in the second quadrant of the complex plane.

Since $\mathcal{O}\left[\mathrm{Re}\left(k_0^f\right)\right] \gg \mathcal{O}\left[\mathrm{Im}\left(k_0^f\right)\right]$, k_0^f is associated with left- and right-propagating wave modes in Ω^f. On the contrary, $\mathcal{O}\left[\mathrm{Re}\left(k_n^f\right)\right] \ll \mathcal{O}\left[\mathrm{Im}\left(k_n^f\right)\right]$ for $n > 0$: these modes are associated with exponentially decaying wave modes. Finally, $\mathcal{O}\left[\mathrm{Re}\left(k_n^f\right)\right] = \mathcal{O}\left[\mathrm{Im}\left(k_n^f\right)\right]$ for $n \in \{-2, -1\}$, so these two roots are associated with attenuating, propagating wave modes. Details on these behaviours can be found in Williams et al. (2013). In the special case where $\gamma = 0$ (purely elastic floes) then k_0^f is a positive real number, k_{-1}^f is in the first quadrant of the complex plane, $k_{-2}^f = -\overline{k_{-1}^f}$, and $\{k_n^f \mid n > 0\}$ are purely imaginary numbers with positive imaginary part. We note that when $1 - \frac{\omega^2 d}{g}$ becomes negative (large frequencies or thicknesses), instead of having the three distinct roots k_{-2}^f, k_{-1}^f and k_0^f, Eq. (10) may admit one double root or one triple root (Williams, 2006, p. 39). Therefore, we enforce $\omega \leq \sqrt{\frac{g}{d}}$ in this study to avoid this issue. For an ice thickness of $1\,\mathrm{m}$, it corresponds to a minimum admissible period of approximately $1.90\,\mathrm{s}$.

https://doi.org/10.5194/tc-2021-391
Preprint. Discussion started: 23 December 2021

The Cryosphere Discussions
Open Access
EGU

For any wave mode n, floe j radiates four waves: two from its left edge (with coefficients $c^{w-}_{j,n}$, $c^{f+}_{j,n}$) and two from its right edge (with coefficients $c^{w+}_{j,n}$, $c^{f-}_{j,n}$) with the exception of the leftmost, semi-infinite floe ($j = N_f$) whose right edge is ignored. The coefficients $c^{w+}_{-1,n}$ and $c^{f-}_{N_f,n}$ are prescribed and represent the right-travelling incident wave forcing in Ω^w_0 and the absence of forcing in $\Omega^f_{N_f}$, respectively: only $c^{w+}_{-1,0} = -i\frac{g}{\omega}a$ is non-zero. The quantity $\theta = \theta^{w+}_{-1,0}$ is an arbitrary phase associated with the forcing. We also note that $\{\theta^{w+}_{-1,n} \mid n > 0\}$ and $\{\theta^{f-}_{N_f,n} \mid n \geq -2\}$ do not take part in the computation and are left undefined. The remaining phases are determined to cancel out exponential terms in Eq. (8) when evaluating ϕ at the edge radiating the wave, i.e.

$$\theta^{w+}_{j,n} = k^w_n (x_j + L_j) \quad ; \quad \theta^{w-}_{j,n} = k^w_n x_j \quad ; \quad \theta^{f+}_{j,n} = k^f_n x_j \quad ; \quad \theta^{f-}_{j,n} = k^f_n (x_j + L_j)\,. \tag{11}$$

Finally, the functions

$$\zeta^w_n(z) = \frac{\cosh(k^w_n(H+z))}{\cosh(k^w_n H)},\ z \in [-H, 0] \quad ; \quad \zeta^f_n(z) = \frac{\cosh(k^f_n(H+z))}{\cosh(k^f_n(H-d))},\ z \in [-H, -d] \tag{12}$$

are vertical basis functions in the free-surface sub-domains and the ice-covered sub-domains, respectively.

3.1.1 Scattering by one floe edge

We obtain the solution to the multiple scattering problem of the incident wave by the ice floes by imposing continuity of pressure and normal velocity across the vertical boundaries between adjacent ice-free and ice-covered sub-domains, i.e. at each floe edge. These conditions are enforced by matching ϕ and $u = \frac{\partial \phi}{\partial x}$ on both sides of each interface. The single edge matching problem is solved using an integral equation method, as described by Williams and Porter (2009) and Mosig (2018).

Considering the scattering by the left edge of floe j and assuming knowledge of $c^{w+}_{m-1,n}$ and $c^{f-}_{m,n}$, the method generates a set of scattering relations relating these incident wave modes coefficients to those associated with wave modes propagating or decaying away from the edge, $c^{f+}_{j,n}$ and $c^{w-}_{j,n}$. When truncating the series in Eq. (8) to N_v evanescent modes, the relations can be summarised by the matrix equation

$$\begin{pmatrix} \boldsymbol{c}^{f+}_j \\ \boldsymbol{c}^{w-}_j \end{pmatrix} = \begin{pmatrix} \mathbf{T}^{fw}_j & \mathbf{R}^f_j \\ \mathbf{R}^w_j & \mathbf{T}^{wf}_j \end{pmatrix} \begin{pmatrix} \mathbf{S}^w_j & \mathbf{0} \\ \mathbf{0} & \mathbf{S}^f_j \end{pmatrix} \begin{pmatrix} \boldsymbol{c}^{w+}_{j-1} \\ \boldsymbol{c}^{f-}_j \end{pmatrix}. \tag{13}$$

where $\mathbf{T}^{fw} \in \mathbb{C}_{N_v+3 \times N_v+1}$, $\mathbf{T}^{wf} \in \mathbb{C}_{N_v+1 \times N_v+3}$, $\mathbf{R}^f \in \mathbb{C}_{N_v+3 \times N_v+3}$, $\mathbf{R}^w \in \mathbb{C}_{N_v+3 \times N_v+3}$ are matrices respectively describing transmission and reflection of waves in either directions through the floe edge, $\boldsymbol{c}^{w\pm}_j = \left(c^{w\pm}_{j,0}, \ldots, c^{w\pm}_{j,N_v}\right)^{\mathrm{T}}$, $\boldsymbol{c}^{f\pm}_j = \left(c^{f\pm}_{j,-2}, \ldots, c^{f\pm}_{j,N_v}\right)^{\mathrm{T}}$ are vectors of unknown coefficients, and $\mathbf{S}^w \in \mathbb{C}_{N_v+1 \times N_v+1}$, $\mathbf{S}^f \in \mathbb{C}_{N_v+3 \times N_v+3}$ are diagonal phase shift matrices.

By symmetry, the scattering by the right edge of floe j is described by

$$\begin{pmatrix} \boldsymbol{c}^{w+}_j \\ \boldsymbol{c}^{f-}_j \end{pmatrix} = \begin{pmatrix} \mathbf{T}^{wf}_j & \mathbf{R}^w_j \\ \mathbf{R}^f_j & \mathbf{T}^{fw}_j \end{pmatrix} \begin{pmatrix} \mathbf{S}^f_j & \mathbf{0} \\ \mathbf{0} & \mathbf{S}^w_{j+1} \end{pmatrix} \begin{pmatrix} \boldsymbol{c}^{f+}_j \\ \boldsymbol{c}^{w-}_{j+1} \end{pmatrix}. \tag{14}$$

https://doi.org/10.5194/tc-2021-391
Preprint. Discussion started: 23 December 2021

The reflection and transmission matrices depend only on the quantities present in the dispersion relations, Eqs. (9) and (10). We note that in the arrangement considered here, these quantities are the same for every floe: the matrices need only be computed once. Our model can however handle a general case with floes of varying thicknesses, flexural rigidities, densities and viscosities. The information carried by the positions and dimensions of the floes are encapsulated in the phase shift matrices which are truly floe-dependent.

A sensitivity analysis (not shown here) proved $N_v = 2$ to be adequate in terms of convergence. Therefore, we use it in the rest of this study.

3.1.2 Scattering by an array of floes

Wave fields radiated by adjacent floes are coupled, which is clearly shown by Eqs. (13) and (14). To solve the multiple scattering problem described by these equations, we take advantage of the sparsity of the matrix representing the combined linear system, using a dedicated solver (Demmel et al., 1999; Virtanen et al., 2020). Specifically, we solve

$$\mathbf{M}\boldsymbol{c} = \boldsymbol{f} \tag{15}$$

where $\mathbf{M}$ is a tridiagonal block matrix and $\boldsymbol{c}$ the vector of unknown potential coefficients.

An array of $N_f + 1$ *finite* floes leads to the matrix

$$\tilde{\mathbf{M}} = \begin{pmatrix} \mathbf{M}_0 & \mathbf{U}_1 & \mathbf{0} & \cdots & \mathbf{0} \\ \mathbf{L}_1 & \mathbf{M}_1 & \mathbf{U}_2 & & \vdots \\ \mathbf{0} & \mathbf{L}_2 & \mathbf{M}_2 & \ddots & \mathbf{0} \\ \vdots & & \ddots & \ddots & \mathbf{U}_{N_f} \\ \mathbf{0} & \cdots & \mathbf{0} & \mathbf{L}_{N_f} & \mathbf{M}_{N_f} \end{pmatrix} \tag{16}$$

with each block element of $\tilde{\mathbf{M}}$ is a square matrix of size $4(N_v + 2)$; $\mathbf{0}, \mathbf{1}$ denote 0-filled matrices and identity matrices, respectively, with sizes compatible with other matrices in the same rows and columns.

As the last floe is here *infinite*, we obtain $\mathbf{M}$ introduced in Eq. (15) by trimming down $\tilde{\mathbf{M}}$ from its last $2(N_v + 2)$ rows and columns. While the size of $\mathbf{M}$ is $[2(N_v + 2)(2N_f + 1)]^2$, it has only $4(N_v + 2)\left[N_f(2N_v + 5) + \frac{1}{2}\right]$ non-zero elements: this number grows linearly with N_f, instead of quadratically.

The vector of unknown coefficients is

$$\boldsymbol{c} = \begin{pmatrix} \boldsymbol{c}_0 & \cdots & \boldsymbol{c}_{N_f-1} & \boldsymbol{c}_{N_f}^{w-} & \boldsymbol{c}_{N_f}^{f+} \end{pmatrix}^T, \text{ with } \boldsymbol{c}_j = \begin{pmatrix} \boldsymbol{c}_j^{w-} & \boldsymbol{c}_j^{f+} & \boldsymbol{c}_j^{f-} & \boldsymbol{c}_j^{w+} \end{pmatrix}^T, \tag{17}$$

and the forcing term

$$\boldsymbol{f} = e^{i\theta} \begin{pmatrix} \mathbf{R}_0^w \boldsymbol{c}_{-1}^{w+} & \mathbf{T}_0^{wf} \boldsymbol{c}_{-1}^{w+} & \mathbf{0} & \cdots & \mathbf{0} \end{pmatrix}^T. \tag{18}$$

Building $\mathbf{M}$ and $\boldsymbol{f}$ and solving for $\boldsymbol{c}$ is linear in time for $\mathcal{O}(N_f) > 10$. For $N_f = 10^5$, these operations are done in around $10\,\mathrm{ms}$ on an Intel Core i5-6300U 2016 laptop. Solving Eq. (15) for $\boldsymbol{c}$ fully determines the spatial part of the potential field in Ω.

https://doi.org/10.5194/tc-2021-391
Preprint. Discussion started: 23 December 2021

3.2 Breakup parametrisation

To parametrise the breakup, we build upon the commonly used strain-based approach (e.g., Kohout and Meylan, 2008; Horvat and Tziperman, 2015). When using the plane stress approximation and our symmetry assumption, the strain $\tilde{\varepsilon}_j$ undergone by ice floe j is

$$\tilde{\varepsilon}_j\left(x', z'\right) = -z' \frac{\partial^2 w}{\partial x'^2} \tag{19}$$

where (x', z') describes a coordinate system local to the floe, defined as $x' = x - x_j$ and $z' = z - \left(\frac{h}{2} - d\right) = z - h\left(\frac{1}{2} - \frac{\rho}{\rho_0}\right)$, hence setting the origin on the intersection of the floe's left edge and horizontal middle surface. Under the plane stress approximation, the vertical displacement field undergone by the floe, $w(x,t)$, does not depend on z': $w(x,t) = \eta(x,t)$. As $|z'| \leq \frac{h}{2}$, the maximum (in absolute value) strain, ε_j, is located on either surface of the floe, i.e. $z' = \pm\frac{h}{2}$. It follows that

$$\varepsilon_j\left(x'\right) = \frac{h}{2}\left|\frac{\partial^2 \eta}{\partial x'^2}\right| = \frac{hT}{4\pi}\left|\mathrm{Re}\left[i \frac{\partial^2}{\partial x'^2}\frac{\partial \phi}{\partial z}\right]\right| \tag{20}$$

with $T = \frac{2\pi}{\omega}$ the wave period.

Floe j is set to break when

$$\max_{x' \in [0, L_j]} \varepsilon_j\left(x'\right) > \varepsilon_c \tag{21}$$

where ε_c is an empirically determined strain threshold.

We situate the breakup point at

$$x_b = \operatorname{argmax} \varepsilon_j \tag{22}$$

so that a floe of length L_j is turned into two floes of length x_b and $L_j - x_b$. Hence, the number of floes at most doubles, if all the floes break in a single simulation.

3.3 Numerical experiment set-up

The values of the parameters kept fixed across all simulations are given in Table 1. Our experiments unwind as follows:

1. The model is initialised with a set of physical parameters as input and a single, semi-infinite floe.
2. The scattered wave field is determined and the strain field evaluated for every floes in the domain. All the floes for which the conditions for breakup are met are split and the domain is updated.
3. The second step is repeated until none of the floes breaks or a prescribed number of iterations reached.

These steps are summarized in Fig.2. The output is the set of coordinate-length pairs describing the final geometry.

For a given iteration, all floes are scrutinised for breakup first, then their positions are updated. To prevent floes from overlapping, they are assigned random new locations, preserving their order. As we do not build any energy dissipation mechanism

https://doi.org/10.5194/tc-2021-391
Preprint. Discussion started: 23 December 2021

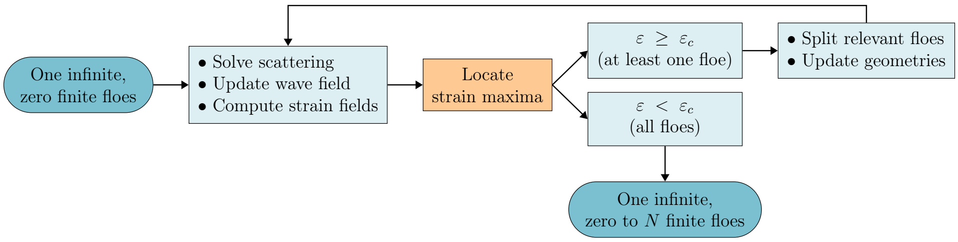

Figure 2. Outline of the numerical experiment.

Table 1. Fixed model parameters and their values.

Symbol	Name	Value
g	Acceleration of gravity	$9.8\,\mathrm{m\,s^{-2}}$
ρ	Ice density	$922.5\,\mathrm{kg\,m^{-3}}$
γ	Ice viscosity	$20\,\mathrm{Pa\,s\,m^{-1}}$
ν	Ice Poisson's ratio	0.3
Y	Ice Young's modulus	$6\,\mathrm{GPa}$
ρ_w	Ocean density	$1025\,\mathrm{kg\,m^{-3}}$
H	Ocean depth	$2400\,\mathrm{m}$

for the fluid in Ω^w, the width of the gap between the floes impacts the phase of the wave, but not its amplitude as it reaches floe $j+1$ after transmission by floe j. Thus, whether floe $j+1$ breaks or not is unlikely to be affected by this gap, but the breakup location is. To account for this introduced randomness, we run each simulation as an ensemble with 50 separate realisations. We ran a sensitivity analysis (not shown here) to confirm that the choice of the parameters governing the random placement does not affect the resulting distribution of floe lengths and removes the potential effect of local resonances in any single realisation.

The final result extracted from the simulation is the set of newly formed floe lengths, excluding the semi-infinite floe on the right of the domain, considered as a steady state FSD.

4 Monochromatic forcing

Before considering the spectrum parametrisation we develop in Sect. 5, we investigate the FSD our model generates under monochromatic forcing with prescribed wave period T, corresponding to angular frequency $\omega = \frac{2\pi}{T}$. In addition to wave frequency, we seek to characterise the effect of the ice thickness h and the strain breakup threshold ε_c on the FSD. Figure 3 (a,b) show example histograms of FSDs obtained for $T = 8\,\mathrm{s}$ and $a = 50\,\mathrm{cm}$, while Fig. 3 (c,d) show the influence of T on the FSD dispersion. Strain threshold in the range 3×10^{-5} to 8.5×10^{-5} have been reported from scarce field measurements (Kohout and Meylan, 2008).

https://doi.org/10.5194/tc-2021-391
Preprint. Discussion started: 23 December 2021

The Cryosphere Discussions

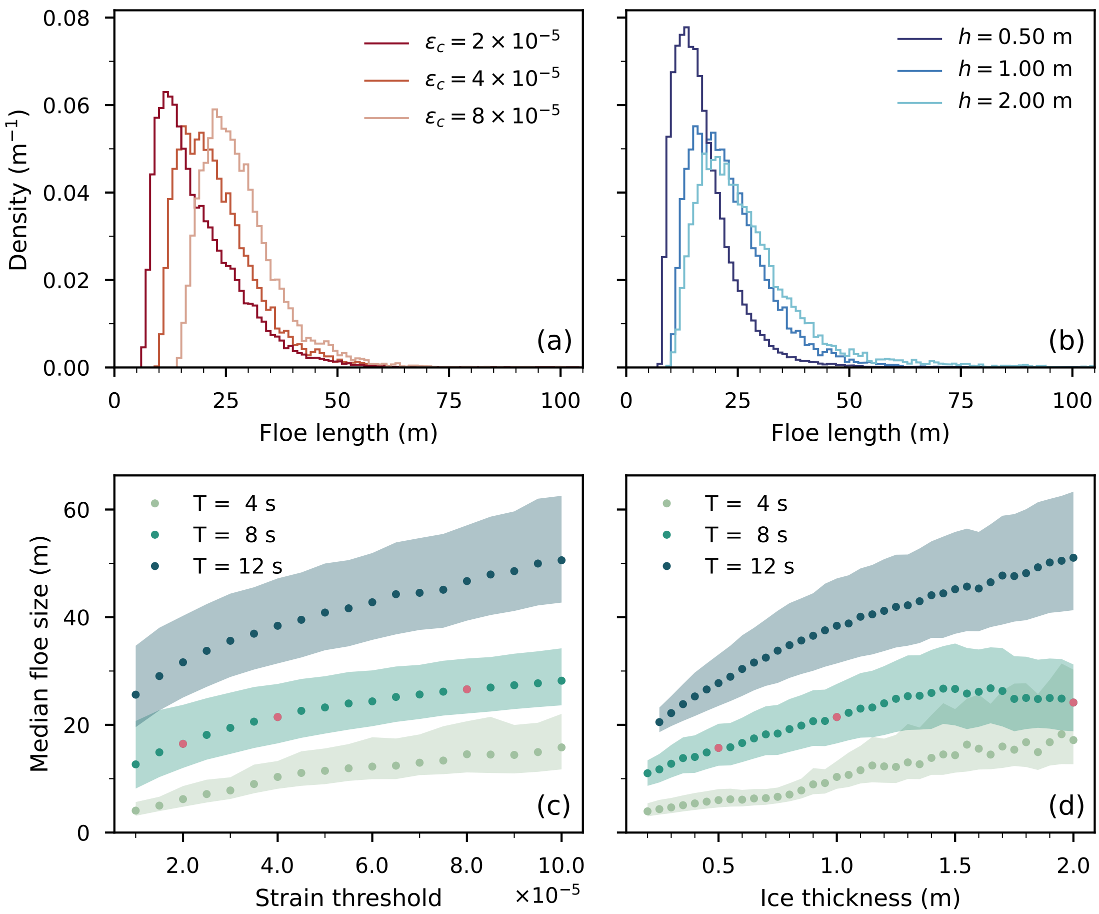

Figure 3. Impact of varying T, ε_c and h on the FSD with $a = 50\,\mathrm{cm}$. (a) Histograms of the floe length for different ε_c. The bin width is $1\,\mathrm{m}$ and $T = 8\,\mathrm{s}$. (b) Same as (a) but for different h. (c) Evolution of the median floe size, when increasing ε_c, for different T. The shaded area indicates the corresponding interquartile range. (d) Same as (c) but for increasing h. In (a,c) $h = 1\,\mathrm{m}$; in (b,d) $\varepsilon_c = 4 \times 10^{-5}$. In the lower panels, the contrasting dots indicate the values plotted in the corresponding top panels. All plotted quantities are ensemble averages over 100 realisations.

We obtain right-skewed distributions, with a positive relationship between the ice mechanical resistance (either through its thickness or its strain threshold before failure) and the presence of larger floes. Qualitatively, increasing ε_c has only a moderate effect on the FSD and seems to be only affecting its mode, shifting it towards larger floes, while its shape remains the same. However, increasing h not only shifts the distribution in a similar way, but also widens its spread and thickens its tail. For both these variables, the median floe size tends to increase and the interquartile range to widen with increasing T, as shown in Fig. 3 (c,d). In addition, for a fixed T, the median floe size increases steadily with ε_c or h, confirming the behaviour observed

https://doi.org/10.5194/tc-2021-391
Preprint. Discussion started: 23 December 2021

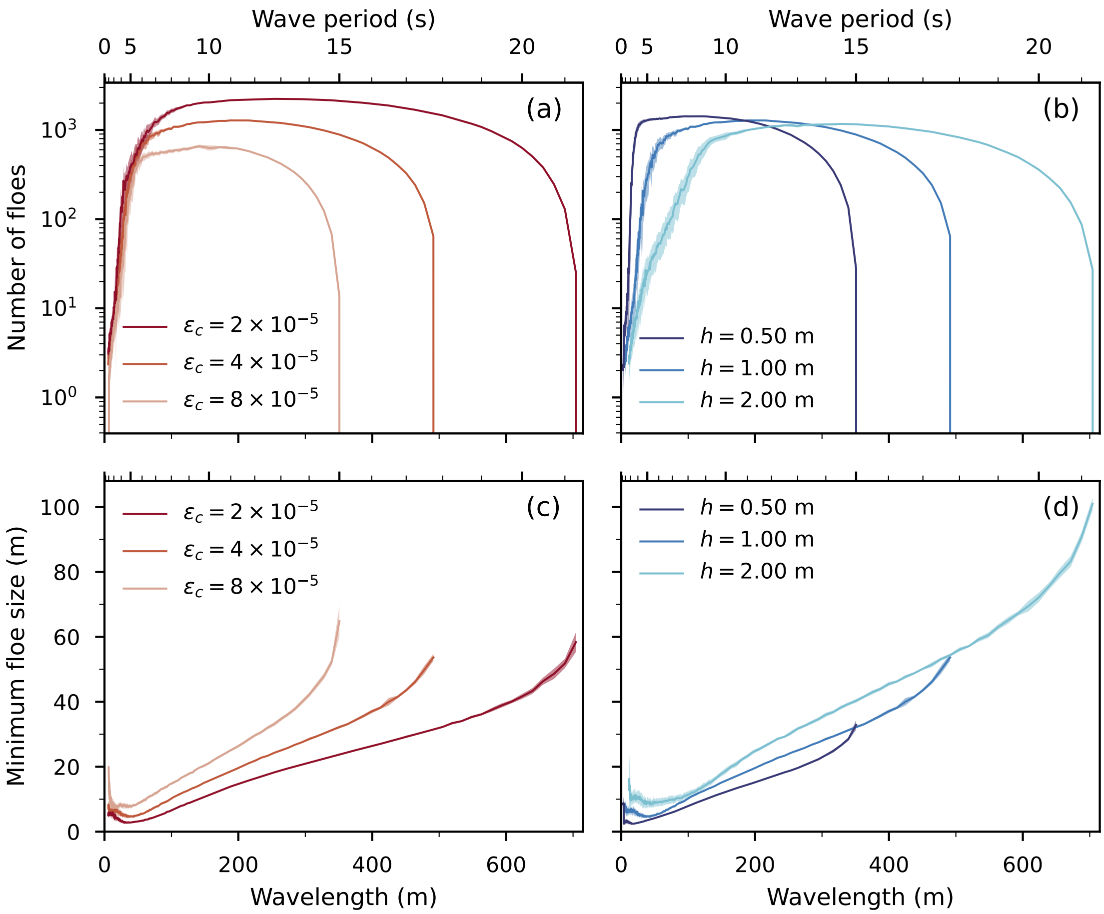

Figure 4. (a) Number of floes at the end of a simulation for different ε_c. (b). Same as (a) but for different h. (c) Minimum floe size in a sample for different ε_c. (d) Same as (c) but for different h. In (a,c) $h = 1\,\text{m}$; in (b,d) $\varepsilon_c = 4 \times 10^{-5}$; $T = 8\,\text{s}$ for all panels. The wavelength axis corresponds to the open-water propagating wavelength at a given T. The plotted lines are ensemble average, the shaded areas indicate one standard deviation.

in the histograms. The dispersion in floe sizes does remain constant for increasing ε_c, at the exception of the shortest waves, while it increases with h. The dispersion is also enhanced for longer waves.

The final number of floes (number of floes reached when the forcing wave field no longer breaks any floe during a simulation) depends sharply on T, as shown on Fig. 4 (a,b). Three regimes can be identified: a crisp increase with T for lower periods (higher frequencies), then a plateau phase, preceding a sudden decrease at higher periods (lower frequencies). The precise delimitations of these regimes depend on the ice properties, and can be explained by the non-linear relationship between T, h, and the undergone strain. Increasing h or T explicitly increases the maximum strain (Eq. (20)). However, increasing T leads to a longer wavelength, translating to a decline in magnitude of the surface curvature term, offsetting the increase. Additionally,

https://doi.org/10.5194/tc-2021-391
Preprint. Discussion started: 23 December 2021

waves propagate with a longer wavelength under the ice than in open water: the thicker the ice, the longer the wavelength becomes. Therefore, increasing h also decreases the surface curvature. Lastly, the fraction of wave energy transmitted by a floe edge, close to 1 for longer waves, drops as period decreases (Fox and Squire, 1990); the precise magnitude of this dip depends on floe length. When considering multiple scattering, these reflections exponentially stack up, making a few floes an effective barrier to low-period waves propagation.

The minimum floe size, shown in Fig. 4 (c,d), also follows three regimes roughly delimited by the same boundaries: a sharp decrease from a local maximum when increasing T from the lowest periods, then a steady growth (appearing to be evolving linearly with the wavelength) from a local minimum, corresponding to the plateau, and a more abrupt increase corresponding to the drop at higher periods. We observe this qualitative behaviour independently from the values of ε_c or h. An increase in minimum floe size with the wavelength is expected. The initial decrease, for shorter wavelength, corresponds to simulations with a very small number of floes: as aforementioned, floes effectively reflect waves of low period.

5 Polychromatic forcing

5.1 Wave spectrum

Our model, as described in Sect. 2 and Sect. 3, parametrises the wave forcing with a single amplitude–frequency pair. To estimate the effect of a developed sea on the FSD f_L, we take the weighted average of distributions resulting from monochromatic model runs, with weights taken from the energy density S of a theoretical ocean spectrum over a truncated frequency interval $[\omega_{\min}, \omega_{\max}]$ so that

$$f_L(l) = \frac{\int_{\omega_{\min}}^{\omega_{\max}} \tilde{f}_L(l,\omega) S(\omega) \mathrm{d}\omega}{\int_{\omega_{\min}}^{\omega_{\max}} S(\omega) \mathrm{d}\omega}. \tag{23}$$

Several parametrisations exist for S; we choose to use a Pierson-Moskowitz spectrum (Pierson and Moskowitz, 1964) as it can be easily adapted to depend only on the significant wave height H_s (Ochi, 2005), giving

$$S(\omega) = c_1 \frac{g^2}{\omega^5} \exp\left(-c_2 \frac{g^2}{\omega^4 {H_s}^2}\right) \tag{24}$$

where $c_1 = 8.1 \times 10^{-3}$, $c_2 = 3.24 \times 10^{-2}$ are non-dimensional constants. This spectrum has been used in previous wave-sea ice interaction studies (e.g., Kohout and Meylan, 2008; Dumont et al., 2011) and is a reduced version of the two-parameter Bretschneider spectrum, used in this context as well (e.g., Horvat and Tziperman, 2015, 2017; Montiel and Squire, 2017).

We evaluate Eq. (23) numerically on 200 linearly spaced frequency bins, setting $H_s = 2a$. As by definition

$$H_s = 4 \sqrt{\int_0^{+\infty} S(\omega) \mathrm{d}\omega}, \tag{25}$$

the bounds of integration $\omega_{\min}$ and $\omega_{\min}$ are set so that the tails $\frac{16}{{H_s}^2} \int_0^{\omega_{\min}} S(\omega) \mathrm{d}\omega = \frac{16}{{H_s}^2} \int_{\omega_{\max}}^{+\infty} S(\omega) \mathrm{d}\omega = 5 \times 10^{-7}$, which captures a significant part of the spectrum. If necessary, $\omega_{\max}$ is adjusted to ensure $\omega \leq \sqrt{\frac{g}{d}}$, as discussed in Sect. 3.1.

https://doi.org/10.5194/tc-2021-391
Preprint. Discussion started: 23 December 2021

The Cryosphere Discussions

For each frequency, we draw an FSD $\tilde{f}_L$ at random from the 50 realisations of this configuration. These FSDs are combined as aforementioned. We repeat (with replacement) this random drawing stage 500 times in order to constitute a distribution ensemble from which statistics can be derived.

5.2 Reference configuration

We consider a reference configuration where $H_s = 1\,\mathrm{m}$, $h = 1\,\mathrm{m}$, $\varepsilon_c = 4\times10^{-5}$; this gives us frequency bounds that correspond to the wave period varying from 1.90 to $9.23\,\mathrm{s}$. In Sect. 5.4, we discuss variations around this scenario.

The resulting FSD, shown in Fig. 5 (a), is remarkably well fitted by a three-parameter lognormal distribution. A random variable L is said to follow such a distribution with parameters μ, σ^2, τ if $\log(L-\tau)$ is normally distributed with mean μ and variance σ^2:

$$L \sim \mathcal{LN}\left(\mu,\sigma^2,\tau\right) \Leftrightarrow \log(L-\tau) \sim \mathcal{N}\left(\mu,\sigma^2\right). \tag{26}$$

The associated density function $f_L(l)$ is positive for $l > \tau$: hence τ is the smallest floe size describable by this statistical model. The scale parameter $s = \exp\mu$ has the physical dimension of the random variable – in this study, a length. The median and the mode of the distribution are given by

$$\text{median} = \tau + s \quad ; \quad \text{mode} = \tau + s\exp\left(\sigma^{-2}\right). \tag{27}$$

More details on the lognormal distribution can be found in Crow and Kunio (1988). In the following, we use the notation $\theta = (s,\sigma,\tau)$ for the parameter vector.

We obtain a point estimate $\hat{\theta}$ with maximum likelihood estimation (see e.g. Azzalini, 1996; Crow and Kunio, 1988). Among the ensemble, $\hat{\theta}$ seems to be normally distributed, with strong correlations between the three parameters and small variances. Therefore, we use the mean vector $\bar{\theta}$ to parametrise an underlying representative lognormal distribution, depicted on Fig. 5 (a,c) as blue lines. The linear combination of lognormal distributions does not have a simplified expression and is not, generally, a lognormal. By defining the mean distribution as a lognormal parametrised with $\bar{\theta}$, we ensure this model is preserved. This can be justified by the low dispersion of $\hat{\theta}$. In that regard, our random sampling aims at providing a confidence interval on the parameters values. The transformation between σ^2 and σ and between μ and s are obviously not linear. However, for the range of values considered here, we find that averaging before or after taking the transformation leads to an absolute relative difference of less than $1\,\%$ (median for s: $4\times10^{-2}\,\%$; median for σ: $4\times10^{-2}\,\%$).

We outline the goodness of fit with a quantile-quantile plot shown in Fig. 5 (b). We standardised the data using (26) before deriving the quantiles, to ease the comparison between the 500 ensemble elements and utilize the symmetry property of the normal distribution. Therefore, an ideal match would have the data lying on the main diagonal. We observe departure from this line for larger floes, the shallower slope suggesting the lognormal parametrisation overpredicts large floes that are not generated by the physical model. However, as $68\,\%$ of the theoretical distribution belong between the ±1 ticks of the horizontal axis, and $95\,\%$ belong between the ±2 ticks, we deem the fit to be excellent. Figure 5 (c) is another visualisation of the goodness of fit, comparing the (strictly speaking, complementary) empirical cumulative distribution functions (CDFs) to the CDF of the

https://doi.org/10.5194/tc-2021-391
Preprint. Discussion started: 23 December 2021

The Cryosphere Discussions
Open Access
EGU

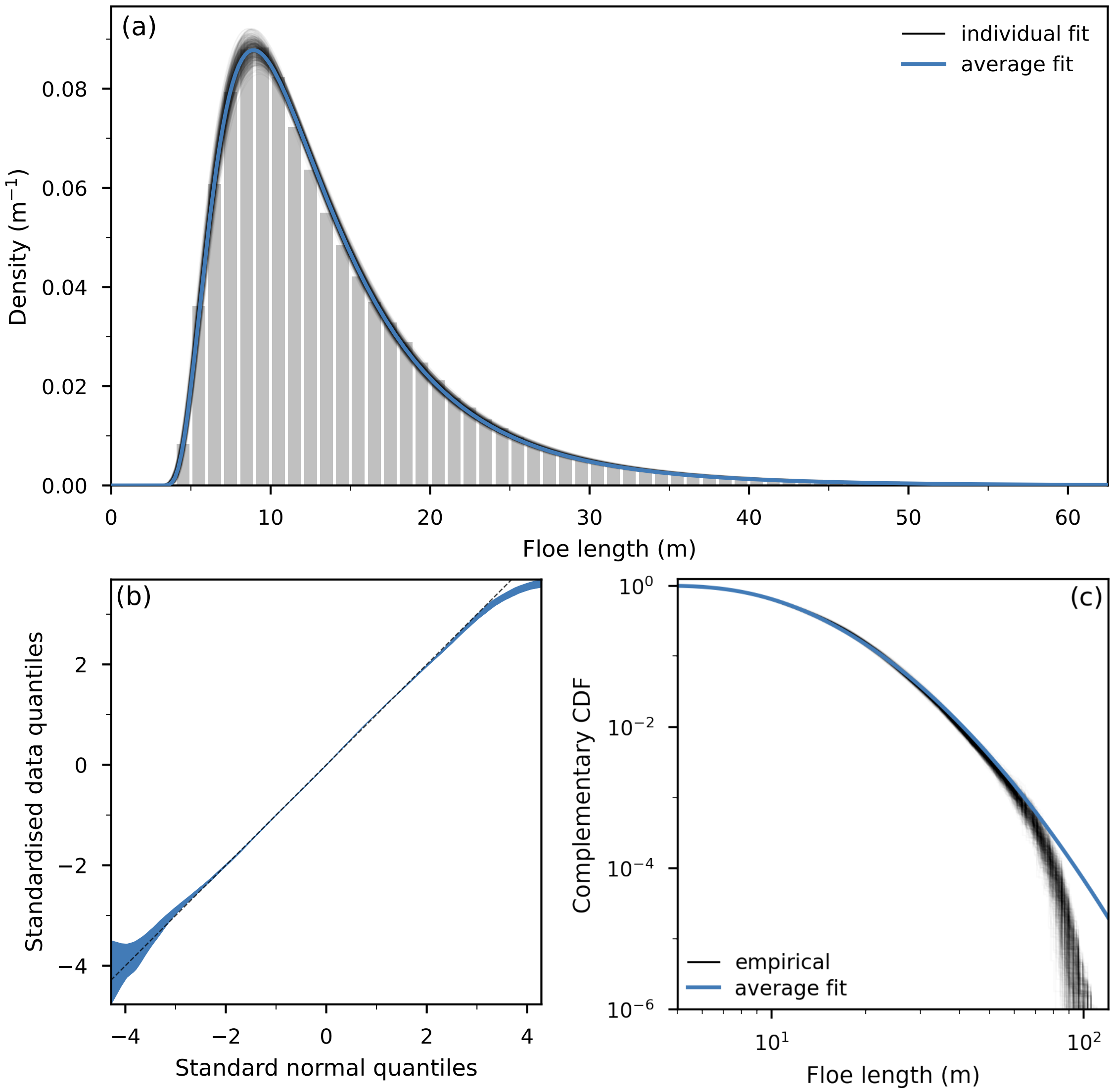

Figure 5. (a) FSDs for the reference configuration: lognormal fits to separate ensemble elements (thin black lines) and average distribution as detailed in text (thicker blue line). The underlying histogram depicts the ensemble average distribution. (b) Normal quantile-quantile plots of the standardised data: the coloured area corresponds to one standard deviation around the mean of the quantile-quantile lines; the dashed line indicates the main diagonal. (c) Cumulative FSDs: individual empirical CDFs (thin black lines) and CDF of the average distributions represented in (a) (thicker blue line).

https://doi.org/10.5194/tc-2021-391
Preprint. Discussion started: 23 December 2021

theoretical average lognormal distribution. They diverge significantly only from the 10^{-2} tick, indicating agreement for more than 99 % of the range of the data. As shown in Fig. 5 (c), the CDF of a random variable following a lognormal distribution could easily be misinterpreted as piecewise straight lines when represented on a log-log plot. This kind of graph is often used for field observations and is at the root of the ingrained power law or split power law conclusion.

5.3 Sub-domain FSD evolution

We do not expect the FSD to have the same shape all across an ice pack or even across the MIZ. To illustrate this effect, we analyse the evolution of the distribution when considering a subset of the domain.Because of our spectrum parametrisation and our distributions being generated in parallel, the definition of the ice edge is not clear, as it is period-dependent. Therefore, we use a sliding window with bounds relative to the total length of ice in each period category. We estimate the density $\tilde{f}_{L;b_\text{inf}-b_\text{sup}}$, with $0 \leq b_\text{inf} < b_\text{sup} \leq 1$, not on all floe lengths $\{L_j \mid j \in \{0, \ldots, N_f - 1\}\}$ but on the subset

$$\left\{ L_j \mid b_\text{inf} < \frac{\Lambda_j}{\Lambda} \leq b_\text{sup} \right\} \tag{28}$$

where $\Lambda_j = \sum_{m=0}^{j} L_m$ is the cumulated floe size up to floe j and $\Lambda = \Lambda_{N_f-1}$ is the total length of finite ice in the domain. We ignore the open water gaps in the process. These monochromatic densities are then combined as detailed in Sect. 5.1. The difference $b_\text{sup} - b_\text{inf}$ gives the width of the sliding window, that we keep fixed at 0.5. The results of this procedure, applied to the reference configuration introduced in Sec. 5.2, are presented in Fig. 6.

The distribution remains right-skewed. Our breakup parametrisation generates floes tending to get smaller as they get further away from the semi-infinite floe marking the right boundary of the domain. This is true across all periods. As a consequence, for increasing b_inf the frequency of larger floes grows, shifting the distribution mode towards larger floes while thickening the distribution tail. This behaviour is similar to the effect of increasing the thickness, presented in Fig. 3 (b).

We considered an alternate window parametrisation based on the ratio $\frac{\Lambda_j}{\max_\omega \Lambda}$. Results were qualitatively similar and we do not attempt to discuss the differences further.

5.4 Forecast based on fitted parameters

We expand the analysis conducted in Sect. 5.2 to other combinations of H_s, h, ε_c. For simplicity, even though we did conduct multivariate simulations, we focus here on investing the effect of varying one variable at a time from their reference values. Hence, when the value of one variable is specified, the other variables assume their reference values, stated in Sect. 5.2. We assess the suitability of fitting the lognormal model though exploratory analysis, as in Sect. 5.2. Histograms of these simulations are presented in Appendix A.

We observe a remarkably good fit over most of the parametric space explored, with a few notable limitations. The smallest waves (significant wave heights between $40\,\text{cm}$ and $60\,\text{cm}$) give rise to different patterns, which we do not analyse further. This is mostly due to them causing small amounts of breakup, leading to a limited number of floes. The empirical distributions obtained with thicker ice ($h > 1.4\,\text{m}$) are less skewed, have a more pronounced peak and thinner tails than the fitted lognormals. Across most configurations, some limitations arise in the tails, with fits for stronger ice overpredicting larger floes, while fits

https://doi.org/10.5194/tc-2021-391
Preprint. Discussion started: 23 December 2021

The Cryosphere Discussions

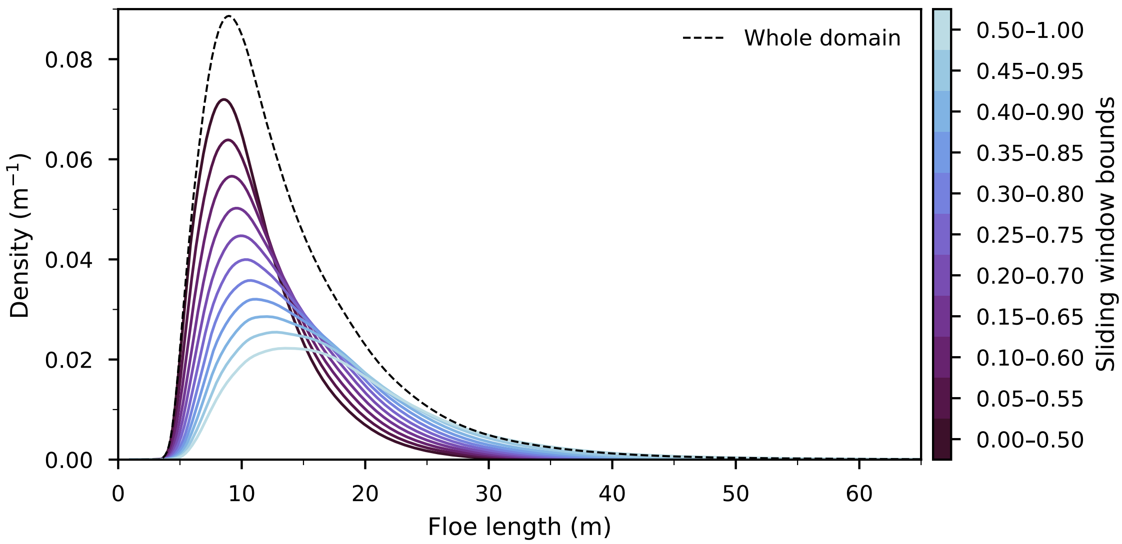

Figure 6. FSDs, estimated by kernel density estimation, in the whole domain and various sub-domains. The area under the partial FSDs are scaled by the number of observations, so that summing the first and the last windows, covering non-overlapping halves of the domain, yields the whole domain FSD. The number of floes, relative to the total number of floes in the domain, decreases steadily from 0.61 to 0.39. Densities averaged over 500 realisations.

for higher waves underpredict them. We report the estimated parameters, averaged over 500 realisations for each configuration, in Fig. 7 (a–i). We note in Fig.7 (g) that $\hat{\tau} < 0$ for large enough wave height, which would allow the model to generate negative floe sizes. This issue will be discussed in the next section. Additionally, we compute the Kolmogorov–Smirnov statistics to further qualify the goodness of fit. The evolution of this statistics is presented in Appendix B.

As can be seen in Fig. 7, the lognormal fit parameters have fairly simple dependences on the physical variables and can be interpolated between computed values, at the exception of the low-amplitude outliers (Fig. 7 (d)). We observe in Fig. 7 (k,l) that the mode of the FSD (see Eq. (27)), or modal floe size, grows with stronger ice, i.e. thicker floes or a larger strain threshold. This behaviour is analogous to the monochromatic case, as reported in Fig. 3. More surprisingly, the modal floe size first decreases with larger waves, reaching a local minimum for $H_s = 1.2\,\mathrm{m}$ before increasing with wave height. As the peak propagating wavelength is proportional to the significant wave height, this non-monotonic evolution does not support wave properties alone govern the dominant floe size, as stated by Herman et al. (2021).

The distribution parameters do not have a clear physical significance by themselves. Beyond the estimation of summary statistics, their main interest is the generation of floe sizes samples without the numerical cost of running the physical model. We illustrate such forecasts, and the associated errors, in Fig. 8. We use the mean distributions, parametrised by $\bar{\theta}$ for each model realisation, to determine the ranges of floe sizes that would be predicted by the lognormal model. Every vertical slice in Fig. 8 (a–c) is a representation of the predicted FSD for the relevant physical variable on the horizontal axis.

https://doi.org/10.5194/tc-2021-391
Preprint. Discussion started: 23 December 2021

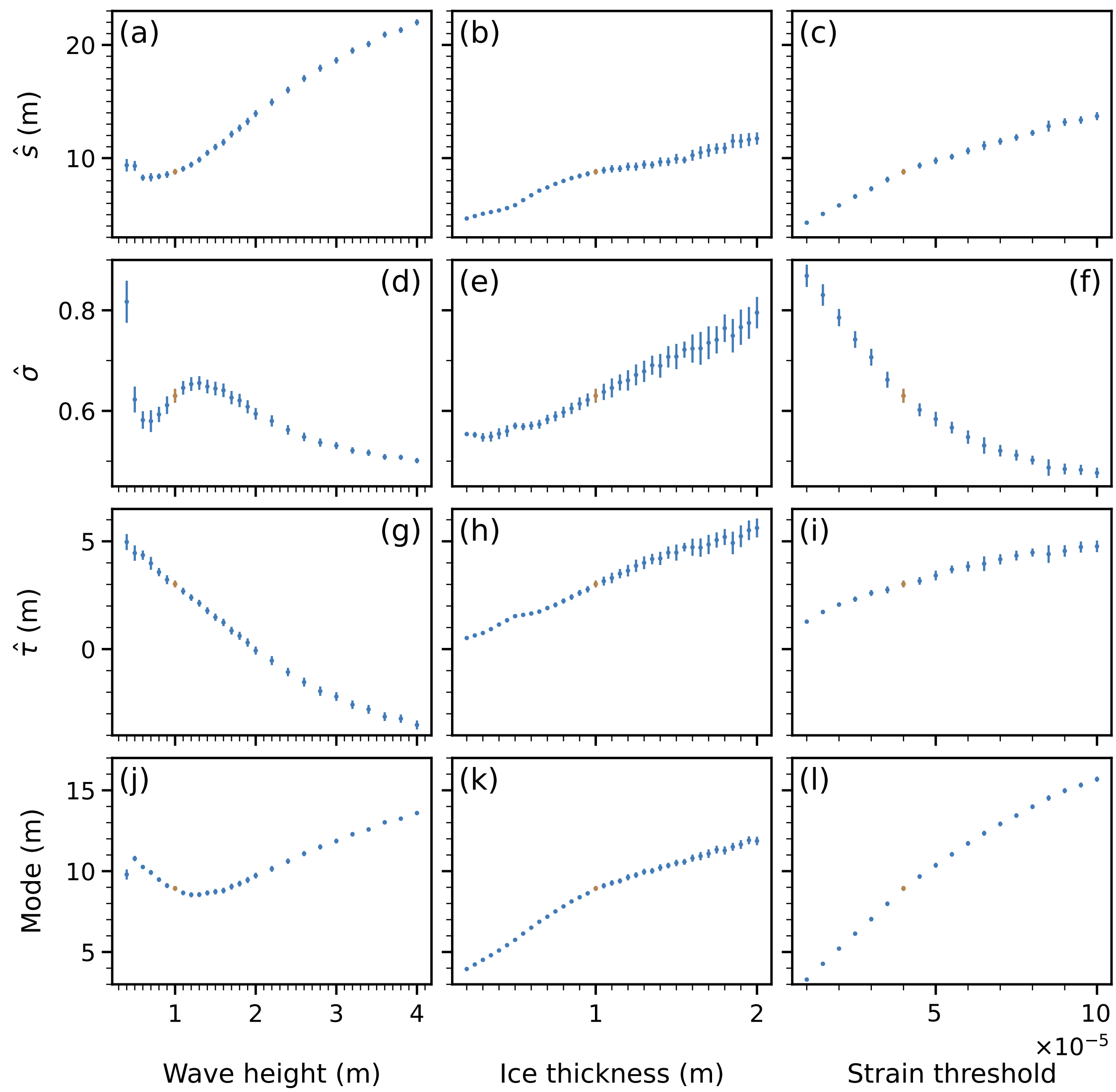

Figure 7. (a–i) Estimated lognormal parameters for different model configurations. (j-l) Distribution mode derived from the estimated parameters. Mean values with one standard deviation error bars. The reference configuration is highlighted with a contrasting colour.

Figure 8 (b,c) again show the dependence of the FSD on h and ε_c lead to a behaviour similar to the monochromatic case. Increasing the ice thickness shifts the median floe size towards larger values and increases the dispersion, the distribution covering a larger span, especially for floes sizes beyond the 75th percentile. The smaller floe categories, below the 50th percentile, are shifted upwards as well and do not contribute to the increasing spread. Increasing the strain threshold sparks a steady increase in median floe size without much effect on the dispersion for $\varepsilon_c \geq 3 \times 10^{-5}$. The prevalence of smaller floes, however, tends to build up slightly. Increasing the significant wave height (hence, indirectly, the peak wavelength) leads to a

https://doi.org/10.5194/tc-2021-391
Preprint. Discussion started: 23 December 2021

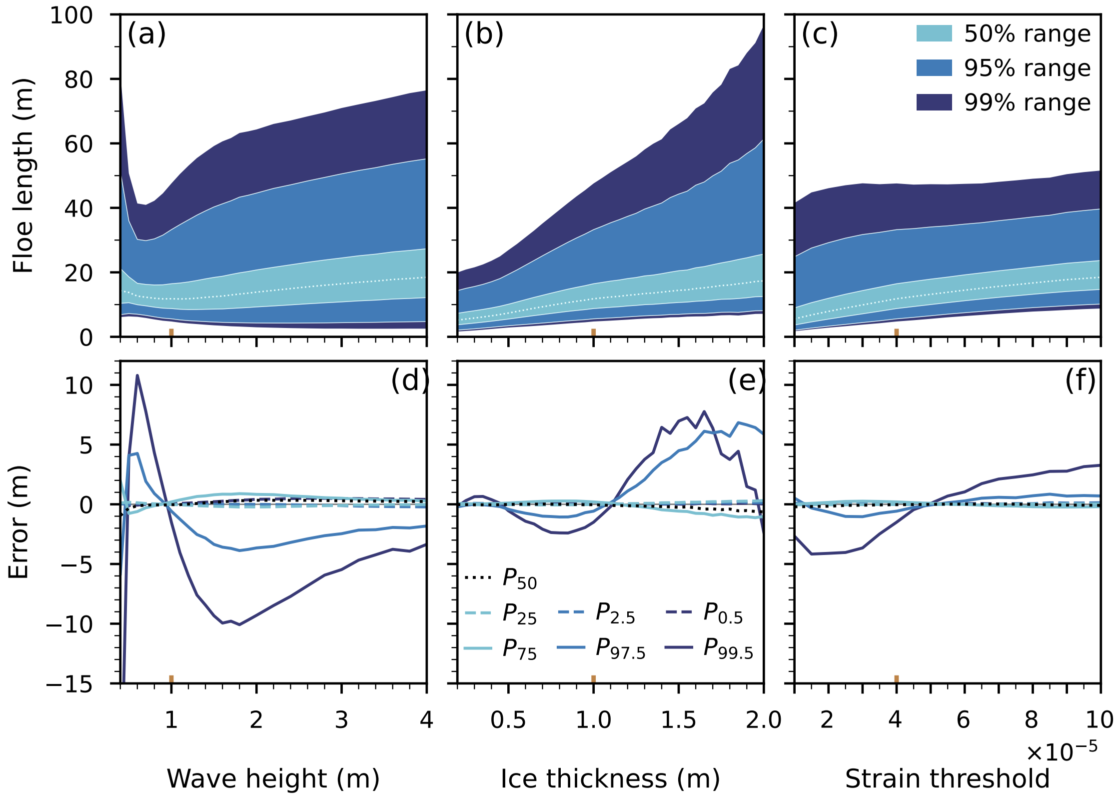

Figure 8. (a–c) Ranges of forecast distributions, generated with mean estimated parameters. The lightest colour area on each panel is the interquartile range; the dotted line denotes the median. The colour areas are symmetrical around the median. (d–f) Errors, with respect to the experimental quantiles, on the forecast quantiles. The represented quantiles bound the colour areas in panels (a–c). The 25th, 50th and 75th percentiles are respectively the first quartile, the median and the third quartile. Negative values suggest over prediction, while positive values suggest under prediction. The reference configuration is highlighted by coloured ticks on the horizontal axes.

more nuanced behaviour. The general trend is an increase dispersion for both small and large floe extremes. There seems to be an inflexion point around $H_s = 1.2\,\mathrm{m}$ for the growth of the 99.5th percentile, this wave height corresponding to the local mode minimum (see Fig. 7 (j)).

Figure 8 (d–f) point out the limitation of the lognormal model by showing the differences between numerical results and statistical predictions for chosen percentiles. As expected, differences arise for more extreme quantiles, corresponding to the long right tail of the distribution. These differences are more pronounced for low wave height and high thickness configurations. The prevalence of extreme floe sizes in the numerical results is, by definition, low. The errors on the three quartiles, are smaller than $1\,\mathrm{m}$ on all the spans of the studied domains. The bulk of the FSD is hence well characterised by the lognormal model.

https://doi.org/10.5194/tc-2021-391
Preprint. Discussion started: 23 December 2021

6 Discussion and conclusions

The emergence of a lognormal FSD from repeated wave-induced breakup is the key outcome of this paper. It contrasts with the power laws often assumed in modelling studies (Williams et al., 2013; Bennetts et al., 2017; Boutin et al., 2020a), or with more narrow distributions from process-based sea ice breakup modelling (Herman, 2017; Montiel and Squire, 2017). Anecdotally, the lognormal distribution has been reported for the size of brash ice pieces in navigation channels (Huang, 1988; Bonath et al., 2019). One of its earliest applications was the description of particles sizes from repeated breakup events (Kolmogoroff, 1941).

This statistical model does come with limitations. Field observations show the extensive spatial variability of the FSD. For instance, Paget et al. (2001) and Inoue (2004) both report an increase in the relative number of small floes when going towards the ice edge, respectively in the Antarctic and the Arctic. Our modelling results mirror this trend, highlighting the difficulty to settle on an all-around FSD parametrisation. We purposely ignore thermal and internal stress effects to focus on the effect of waves on the FSD, so validation with observational data would only be appropriate for a MIZ post wave-induced breakup. As detailed in Sect. 5.4 and illustrated in Fig. 8 (d–f), the distribution struggles to capture the behaviour of the most extreme floe sizes in our simulations. We note, however, that for such floe sizes wave-induced breakup is not likely to be the dominant mechanism governing the evolution of the FSD (Roach et al., 2018). We further found that the lognormal fit is not valid for small waves and the domain of thicknesses we analysed is at the limit of validity, suggesting that even in this simplified setting the lognormal is not universal. Again, in such regimes, thermal and internal stress effects are likely to dominate over wave-induced breakup. Another point of concern is that we have $\hat{\tau} < 0$ for $H_s \geq 2\,\mathrm{m}$, meaning the probability of sampling negatively-sized floe is not 0. Constraining the MLE to yield positive estimates led to poor fit performance. This issue, which concerns a small fraction ($< 10^{-5}$) of the floes, can be easily circumvented by artificially bounding and rescaling the density function.

Additionally to the wave height, the ice thickness and the strain threshold, we analysed the effect of varying the ice viscosity γ (not shown here). We observed a significant contrast between $\gamma = 0$ (purely elastic ice) and $\gamma > 0$. The simulations we run with purely elastic floes are the only ones that reached the maximum number of iterations, set at 1000. It seems that scattering alone is not effective enough at dissipating wave energy, leading to a rapid and sustained growth of the number of floes. However, marginal differences exist between ensuing distributions as long as some viscosity is introduced (γ in 1–$100\,\mathrm{Pa\,s\,m^{-1}}$). Williams et al. (2013) used the same viscosity parametrisation with $\gamma = 13\,\mathrm{Pa\,s\,m^{-1}}$ derived from a 1979 campaign in the Bering Sea, while Mosig et al. (2015) fitted $\gamma = 6\,\mathrm{Pa\,s\,m^{-1}}$ to a 2012 Southern Ocean dataset. We used $\gamma = 20\,\mathrm{Pa\,s\,m^{-1}}$ throughout, which is a bit more conservative but, as stated, does not significantly impact the results. Although associated with the ice, this parameter can be thought of as a parametrisation of the collection of all wave dissipation effects (Montiel et al., 2016).

Clauset et al. (2009) analysed 14 empirical datasets of different continuous variables, originally modelled with power laws, coming from a mixture of research areas. They observe that the power law is statistically appropriate for 8 of these datasets, while the lognormal holds for 13 of them. They use a relative goodness of fit test to show that the lognormal is more suitable than the power law in 12 cases, and significantly so in 4 cases, concluding: “In general, we find that it is extremely difficult

https://doi.org/10.5194/tc-2021-391
Preprint. Discussion started: 23 December 2021

The Cryosphere Discussions

to tell the difference between log-normal and power-law behaviour" (Clauset et al., 2009). Stern et al. (2018) recommended a procedure for analysing floe size data in order to raise awareness of better fit methods, with considering an alternative distribution as an optional step. We believe this study heads in that direction and that the lognormal distribution should be considered as an alternative. Revisiting some of the studies tabulated by Stern et al. (2018) with this hypothesis could shed some light on its validity.

Parametric distributions may never be flawless descriptions of the quantities they model. The power law used by multiple models has some weaknesses, and its materialisation under the action of waves is not established. In this study, we show the relevance of the lognormal distribution when considering wave-induced breakup. We describe the evolution of the distribution shape for a range of ice properties, under various wave forcings. These results aim at being a step towards the parametrisation of wave action in FSD-evolving models.

Code and data availability. The model code, software tools developed for analysis and the resulting preprocessed output presented in this paper are publicly available (Mokus and Montiel, 2021). The raw output is available upon request.

Appendix A: Histograms

Appendix B: Kolmogorov–Smirnov statistics

The Kolmogorov–Smirnov statistics D_{KS} is the largest difference between an empirical cumulative distribution function (CDF) and a reference CDF (Massey, 1951). By definition of the CDF, D_{KS} is bounded by 0 and 1. When the distribution parameters have been estimated from the data, D_{KS} can be used to run a Lilliefors test (Lilliefors, 1967). By comparing D_{KS} to a critical value, depending on sample size and a chosen confidence level, one uses this test to reject a distribution hypothesis – not to confirm it. However, the power of this test, and others, notoriously increases with the sample size, making them able to detect trivial deviations from a reference distribution. This is a simple consequence of the fact that a model cannot perfectly fit the data. Hence, these tests only give a binary answer, not taking into account the usefulness of an imperfect model. A more purposeful alternative consists in studying the relative goodness of fit between different models, which we do not explore in detail here.

Instead of rejecting the lognormal hypothesis at an arbitrarily-chosen confidence level, we report D_{KS} as an indicative performance metric to compare our different configurations. More specifically, for each fitted lognormal with estimated parameters $\hat{\theta}$ (that is, 500 different realisations per model configuration), we generate a random sample of size N_{eff} from the distribution. We use Kish's effective sample size (Kish, 1965), the rounded up ratio of the squared sum of weights to the sum of the squared weights, as N_{eff}. We use maximum likelihood estimation (MLE) to estimate $\hat{\theta}_b$ from this sample, and we compute D_{KS} for this sample and the distribution parametrised by $\hat{\theta}_b$. We then define ΔD_{KS} as the difference between D_{KS} from the random sample and D_{KS} from our data. We repeat these three steps 1000 times to derive the distribution of Δ_{KS} for each model configuration. This is analogous to the bootstrapping method described by Clauset et al. (2009). It ensues that ΔD_{KS} is bounded by -1 and 1,

https://doi.org/10.5194/tc-2021-391
Preprint. Discussion started: 23 December 2021

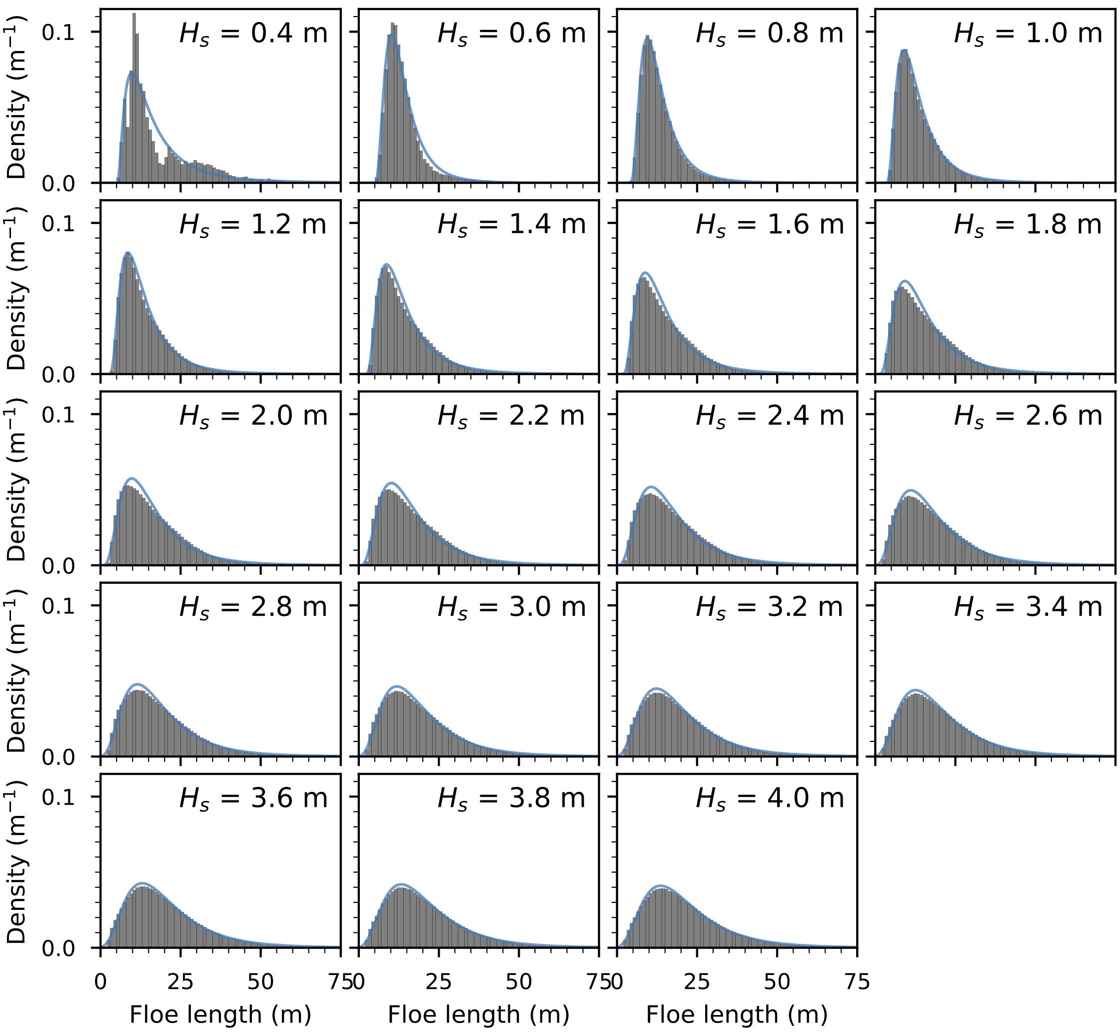

Figure A1. Histograms and average lognormal fits, as described in Sect. 5.2, for varying significant wave height.

with $\Delta D_{\mathrm{KS}} > 0$ indicating cases where our data is fitted by the lognormal model better than data actually lognormally sampled, in terms of distance between the CDFs.

We report the results on Figs. B1–B3. This procedure quantitatively illustrate the conclusions derived from analysing histograms and quantile–quantile plots.

https://doi.org/10.5194/tc-2021-391
Preprint. Discussion started: 23 December 2021

The Cryosphere
Discussions
Open Access

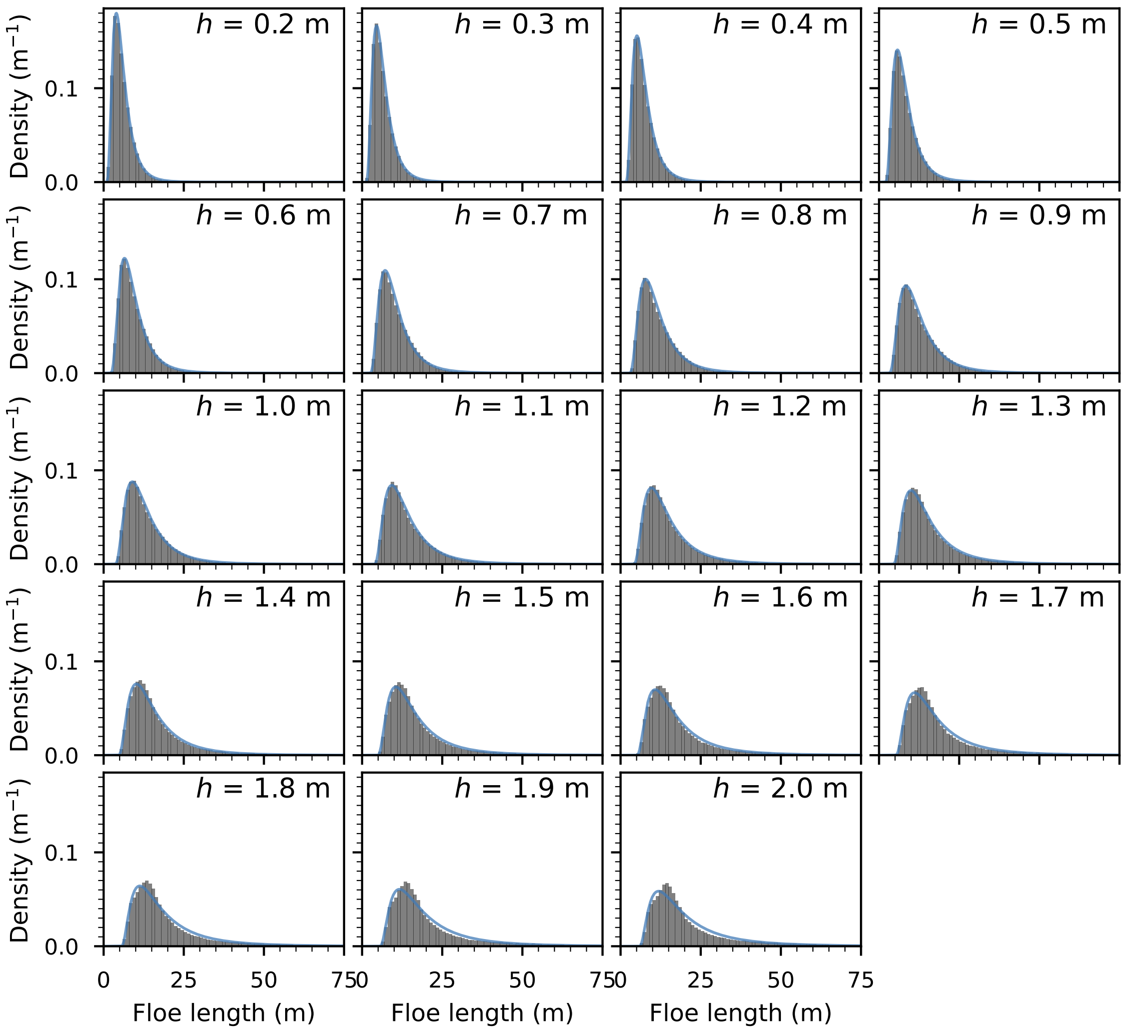

Figure A2. Histograms and average lognormal fits, as described in Sect. 5.2, for varying ice thickness.

https://doi.org/10.5194/tc-2021-391
Preprint. Discussion started: 23 December 2021

The Cryosphere Discussions

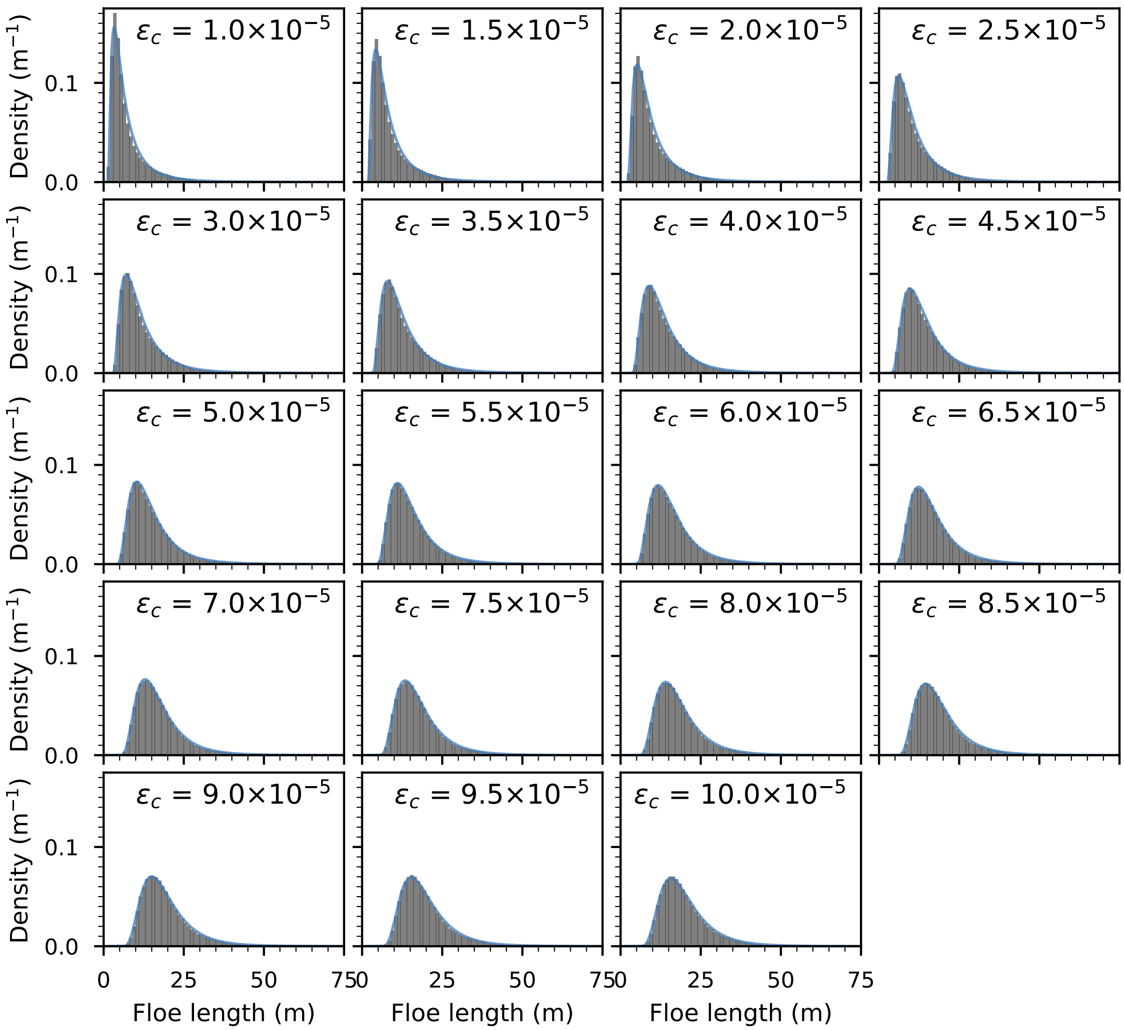

Figure A3. Histograms and average lognormal fits, as described in Sect. 5.2, for varying strain threshold.

https://doi.org/10.5194/tc-2021-391
Preprint. Discussion started: 23 December 2021

The Cryosphere Discussions
Open Access
EGU

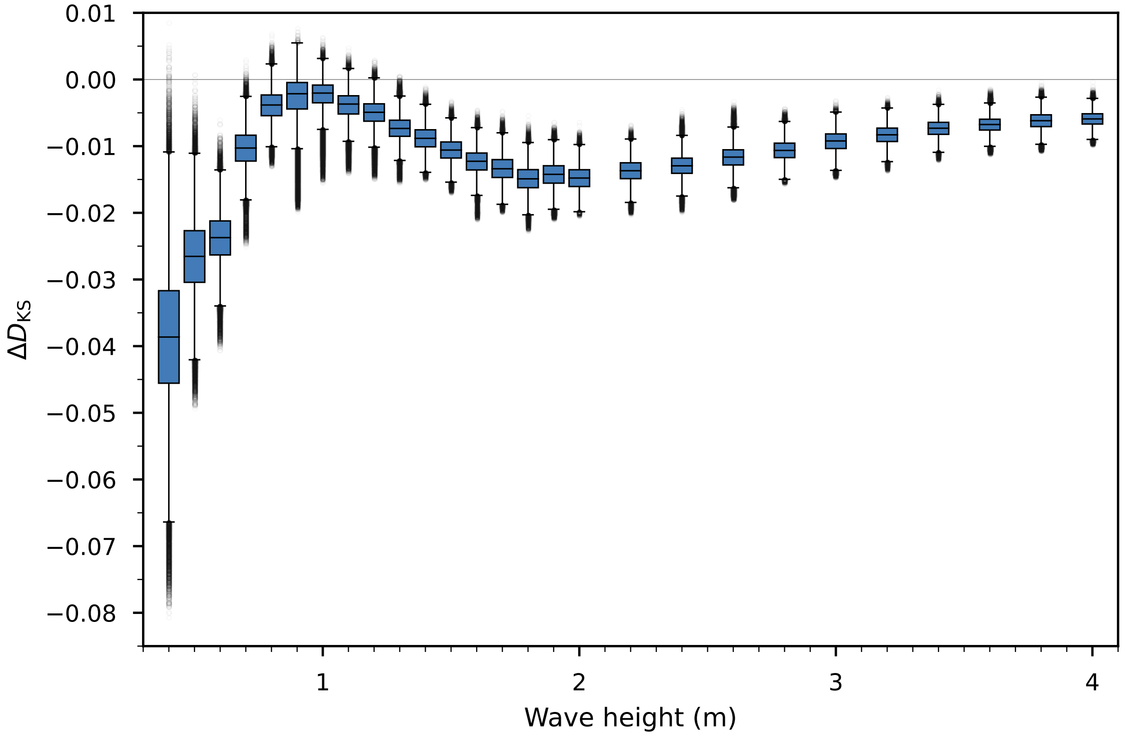

Figure B1. Distribution of ΔD_{KS}, as defined in the text, for varying significant wave height. The boxes are bounded by the first and third quartiles and the black lines are medians. The whiskers lengths is one and a half times the interquartile range. Black circles represent outliers.

https://doi.org/10.5194/tc-2021-391
Preprint. Discussion started: 23 December 2021

The Cryosphere
Discussions

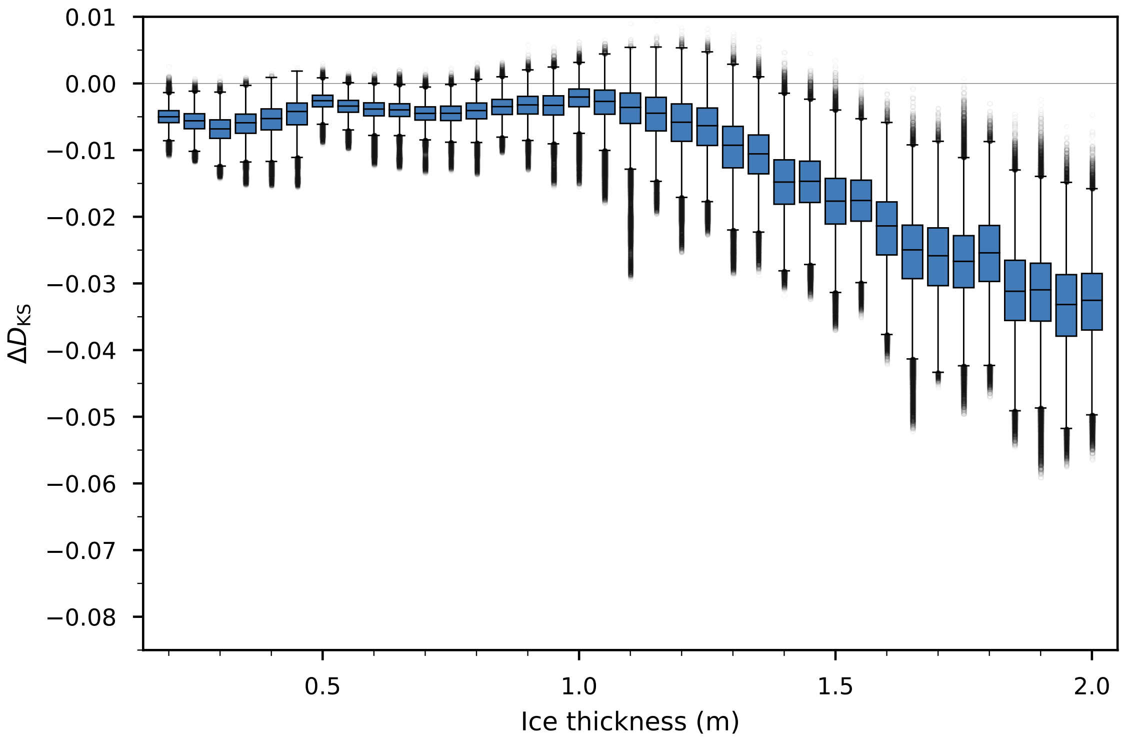

Figure B2. Same as Fig. B1 for varying ice thickness.

https://doi.org/10.5194/tc-2021-391
Preprint. Discussion started: 23 December 2021

The Cryosphere
Discussions
Open Access

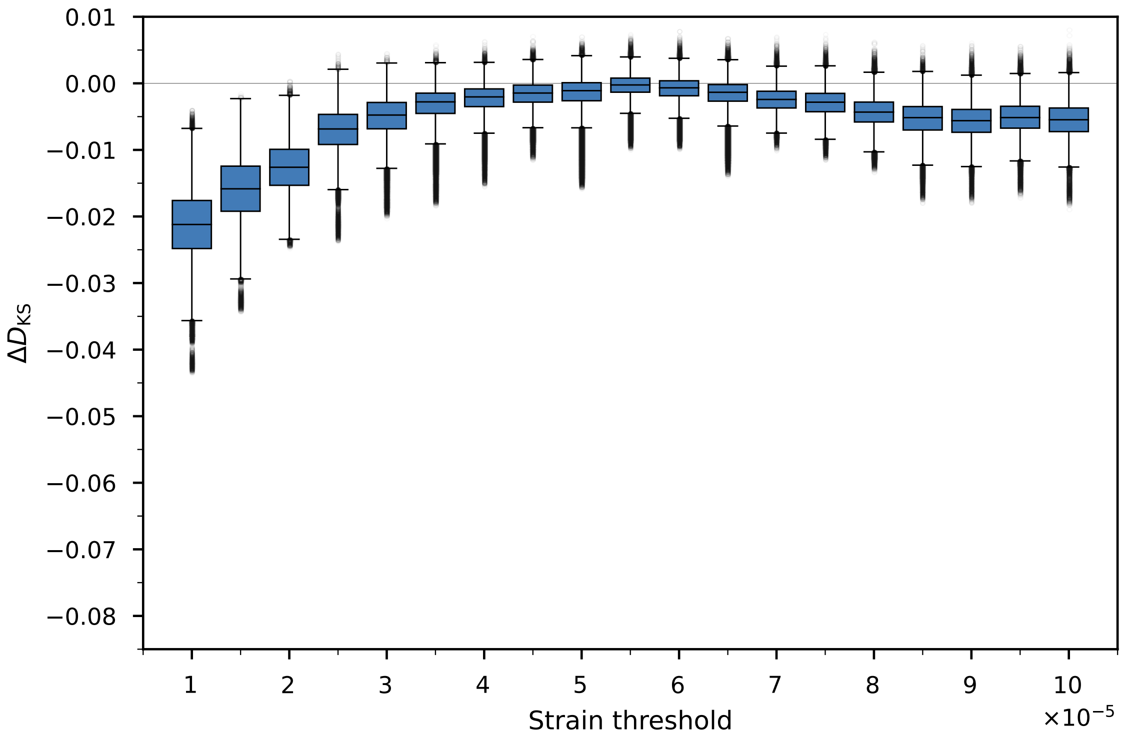

Figure B3. Same as Fig. B1 for varying strain threshold.

https://doi.org/10.5194/tc-2021-391
Preprint. Discussion started: 23 December 2021

The Cryosphere
Discussions
Open Access

Author contributions. NM and FM designed the numerical experiments. NM developed the model code, ran the simulations and conducted the analysis. NM prepared the manuscript with significant inputs from and under the supervision of FM.

Competing interests. The authors declare that they have no conflict of interest.

Acknowledgements. The authors thank Christopher Horvat for proposing the method of combining FSDs obtained at individual frequencies in order to form the FSD resulting from the breakup by a wave spectrum (Eq. (23)). NM acknowledges the financial support from a University of Otago doctoral scholarship. This work was funded by the Marsden Fund, project 18-UOO-216, managed by Royal Society Te Apārangi. FM was also supported by the New Zealand's Antarctic Science Platform (Project 4) and Royal Society Te Apārangi (Marsden project 20-UOO-173).

https://doi.org/10.5194/tc-2021-391
Preprint. Discussion started: 23 December 2021

References

Asplin, M. G., Galley, R., Barber, D. G., and Prinsenberg, S.: Fracture of summer perennial sea ice by ocean swell as a result of Arctic storms, Journal of Geophysical Research: Oceans, 117, n/a–n/a, https://doi.org/10.1029/2011jc007221, 2012.

Azzalini, A.: Statistical inference : based on the likelihood, Monographs on statistics and applied probability ; 68, Chapman & Hall/CRC, Boca Raton ; New York, 1st ed. edn., 1996.

Bennetts, L. G., O'Farrell, S., and Uotila, P.: Brief communication: Impacts of ocean-wave-induced breakup of Antarctic sea ice via thermodynamics in a stand-alone version of the CICE sea-ice model, The Cryosphere, 11, 1035–1040, https://doi.org/10.5194/tc-11-1035-2017, 2017.

Bonath, V., Zhaka, V., and Sand, B.: Field measurements on the behavior of brash ice, in: Proceedings of the 25th International Conference on Port and Ocean Engineering under Arctic Conditions, 2019.

Boutin, G., Ardhuin, F., Dumont, D., Sévigny, C., Girard-Ardhuin, F., and Accensi, M.: Floe Size Effect on Wave-Ice Interactions: Possible Effects, Implementation in Wave Model, and Evaluation, Journal of Geophysical Research: Oceans, 123, 4779–4805, https://doi.org/10.1029/2017jc013622, 2018.

Boutin, G., Lique, C., Ardhuin, F., Rousset, C., Talandier, C., Accensi, M., and Girard-Ardhuin, F.: Towards a coupled model to investigate wave–sea ice interactions in the Arctic marginal ice zone, The Cryosphere, 14, 709–735, https://doi.org/10.5194/tc-14-709-2020, 2020a.

Boutin, G., Williams, T., Rampal, P., Olason, E., and Lique, C.: Wave–sea-ice interactions in a brittle rheological framework, The Cryosphere, https://doi.org/10.5194/tc-2020-19, 2020b.

Castruccio, F. S., Ruprich-Robert, Y., Yeager, S. G., Danabasoglu, G., Msadek, R., and Delworth, T. L.: Modulation of Arctic Sea Ice Loss by Atmospheric Teleconnections from Atlantic Multidecadal Variability, Journal of Climate, 32, 1419–1441, https://doi.org/10.1175/jcli-d-18-0307.1, 2019.

Clauset, A., Shalizi, C. R., and Newman, M. E. J.: Power-Law Distributions in Empirical Data, SIAM Review, 51, 661–703, https://doi.org/10.1137/070710111, 2009.

Collins, C. O., Rogers, W. E., Marchenko, A., and Babanin, A. V.: In situ measurements of an energetic wave event in the Arctic marginal ice zone, Geophysical Research Letters, 42, 1863–1870, https://doi.org/10.1002/2015gl063063, 2015.

Crow, E. L. and Kunio, S.: Lognormal distributions : theory and applications, Statistics, textbooks and monographs ; v. 88, M. Dekker, New York, 1988.

Demmel, J. W., Eisenstat, S. C., Gilbert, J. R., Li, X. S., and Liu, J. W. H.: A Supernodal Approach to Sparse Partial Pivoting, SIAM Journal on Matrix Analysis and Applications, 20, 720–755, https://doi.org/10.1137/s0895479895291765, 1999.

Dolatshah, A., Nelli, F., Bennetts, L. G., Alberello, A., Meylan, M. H., Monty, J. P., and Toffoli, A.: Letter: Hydroelastic interactions between water waves and floating freshwater ice, Physics of Fluids, 30, 091 702, https://doi.org/10.1063/1.5050262, 2018.

Dumas-Lefebvre, E. and Dumont, D.: Aerial observations of sea ice breakup by ship-induced waves, in: ArcticNet Annual Scientific Meeting, https://doi.org/10.13140/RG.2.2.23493.40164, 2020.

Dumont, D., Kohout, A., and Bertino, L.: A wave-based model for the marginal ice zone including a floe breaking parameterization, Journal of Geophysical Research, 116, https://doi.org/10.1029/2010jc006682, 2011.

Dupont, F., Dumont, D., Lemieux, J.-F., Dumas-Lefebvre, E., and Caya, A.: A probabilistic seabed-ice keel interaction model, The Cryosphere Discussions, https://doi.org/10.5194/tc-2021-273, preprint, 2021.

Fox, C. and Squire, V. A.: Reflection and transmission characteristics at the edge of shore fast sea ice, Journal of Geophysical Research, 95, 11 629, https://doi.org/10.1029/jc095ic07p11629, 1990.

Fox, C. and Squire, V. A.: On the oblique reflexion and transmission of ocean waves at shore fast sea ice, Philosophical Transactions of the Royal Society of London. Series A: Physical and Engineering Sciences, 347, 185–218, https://doi.org/10.1098/rsta.1994.0044, 1994.

Herman, A.: Wave-induced stress and breaking of sea ice in a coupled hydrodynamic discrete-element wave–ice model, The Cryosphere, 11, 2711–2725, https://doi.org/10.5194/tc-11-2711-2017, 2017.

Herman, A., Evers, K.-U., and Reimer, N.: Floe-size distributions in laboratory ice broken by waves, The Cryosphere, 12, 685–699, https://doi.org/10.5194/tc-12-685-2018, 2018.

Herman, A., Wenta, M., and Cheng, S.: Sizes and Shapes of Sea Ice Floes Broken by Waves–A Case Study From the East Antarctic Coast, Frontiers in Earth Science, 9, https://doi.org/10.3389/feart.2021.655977, 2021.

Horvat, C. and Tziperman, E.: A prognostic model of the sea-ice floe size and thickness distribution, The Cryosphere, 9, 2119–2134, https://doi.org/10.5194/tc-9-2119-2015, 2015.

Horvat, C. and Tziperman, E.: The evolution of scaling laws in the sea ice floe size distribution, Journal of Geophysical Research: Oceans, 122, 7630–7650, https://doi.org/10.1002/2016jc012573, 2017.

Horvat, C., Tziperman, E., and Campin, J.-M.: Interaction of sea ice floe size, ocean eddies, and sea ice melting, Geophysical Research Letters, 43, 8083–8090, https://doi.org/10.1002/2016gl069742, 2016.

Huang, H.-P.: Ice formation in frequently transited navigation channels, Ph.D. thesis, The University of Iowa, 1988.

Hunke, E., Allard, R., Bailey, D. A., Blain, P., Craig, A., Dupont, F., DuVivier, A., Grumbine, R., Hebert, D., Holland, M., Jeffery, N., Jean-Francois Lemieux, Osinski, R., Rasmussen, T., Ribergaard, M., Roberts, A., Francois Roy, Turner, M., and Worthen, D.: CICE-Consortium/CICE: CICE Version 6, https://doi.org/10.5281/zenodo.1205674, 2021.

Inoue, J.: Ice floe distribution in the Sea of Okhotsk in the period when sea-ice extent is advancing, Geophysical Research Letters, 31, https://doi.org/10.1029/2004gl020809, 2004.

Kish, L.: Survey sampling, 04; HN29, K5., 1965.

Kohout, A. L. and Meylan, M. H.: An elastic plate model for wave attenuation and ice floe breaking in the marginal ice zone, Journal of Geophysical Research, 113, https://doi.org/10.1029/2007jc004434, 2008.

Kolmogoroff, A.: Über das logarithmisch normale Verteilungsgesetz der Dimensionen der Teilchen bei Zerstückelung, in: CR (Doklady) Acad. Sci. URSS (NS), vol. 31, pp. 99–101, 1941.

Kwok, R.: Arctic sea ice thickness, volume, and multiyear ice coverage: losses and coupled variability (1958–2018), Environmental Research Letters, 13, 105 005, https://doi.org/10.1088/1748-9326/aae3ec, 2018.

Kwok, R., Cunningham, G. F., Wensnahan, M., Rigor, I., Zwally, H. J., and Yi, D.: Thinning and volume loss of the Arctic Ocean sea ice cover: 2003–2008, Journal of Geophysical Research, 114, https://doi.org/10.1029/2009jc005312, 2009.

Lilliefors, H. W.: On the Kolmogorov-Smirnov Test for Normality with Mean and Variance Unknown, Journal of the American Statistical Association, 62, 399–402, https://doi.org/10.1080/01621459.1967.10482916, 1967.

Massey, F. J.: The Kolmogorov-Smirnov Test for Goodness of Fit, Journal of the American Statistical Association, 46, 68–78, https://doi.org/10.1080/01621459.1951.10500769, 1951.

Meylan, M. H., Bennetts, L. G., and Kohout, A. L.: In situ measurements and analysis of ocean waves in the Antarctic marginal ice zone, Geophysical Research Letters, 41, 5046–5051, https://doi.org/10.1002/2014gl060809, 2014.

Mokus, N. and Montiel, F.: Model code and simulation results for the investigation of a wave-generated floe size distribution, https://doi.org/10.6084/m9.figshare.17303927, 2021.

Montiel, F. and Squire, V. A.: Modelling wave-induced sea ice break-up in the marginal ice zone, Proceedings of the Royal Society A: Mathematical, Physical and Engineering Science, 473, 20170 258, https://doi.org/10.1098/rspa.2017.0258, 2017.

Montiel, F., Squire, V. A., and Bennetts, L. G.: Attenuation and directional spreading of ocean wave spectra in the marginal ice zone, Journal of Fluid Mechanics, 790, 492–522, https://doi.org/10.1017/jfm.2016.21, 2016.

Montiel, F., Squire, V. A., Doble, M., Thomson, J., and Wadhams, P.: Attenuation and Directional Spreading of Ocean Waves During a Storm Event in the Autumn Beaufort Sea Marginal Ice Zone, Journal of Geophysical Research: Oceans, 123, 5912–5932, https://doi.org/10.1029/2018jc013763, 2018.

Mosig, J. E. M.: Contemporary wave–ice interaction models, Ph.D. thesis, University of Otago, 2018.

Mosig, J. E. M., Montiel, F., and Squire, V. A.: Comparison of viscoelastic-type models for ocean wave attenuation in ice-covered seas, Journal of Geophysical Research: Oceans, 120, 6072–6090, https://doi.org/10.1002/2015jc010881, 2015.

Ochi, M. K.: Ocean waves: the Stochastic Approach, 6, Cambridge University Press, 2005.

Paget, M., Worby, A. P., and Michael, K. J.: Determining the floe-size distribution of East Antarctic sea ice from digital aerial photographs, Annals of Glaciology, 33, 94–100, https://doi.org/10.3189/172756401781818473, 2001.

Parkinson, C. L. and Comiso, J. C.: On the 2012 record low Arctic sea ice cover: Combined impact of preconditioning and an August storm, Geophysical Research Letters, 40, 1356–1361, https://doi.org/10.1002/grl.50349, 2013.

Passerotti, G., Bennetts, L. G., von Bock und Polach, F., Alberello, A., Puolakka, O., Dolatshah, A., Monbaliu, J., and Toffoli, A.: Interactions between irregular wave fields and sea ice: A physical model for wave attenuation and ice break up, 2021.

Perovich, D. K. and Jones, K. F.: The seasonal evolution of sea ice floe size distribution, Journal of Geophysical Research: Oceans, 119, 8767–8777, https://doi.org/10.1002/2014jc010136, 2014.

Pierson, W. J. and Moskowitz, L.: A proposed spectral form for fully developed wind seas based on the similarity theory of S. A. Kitaigorodskii, Journal of Geophysical Research, 69, 5181–5190, https://doi.org/10.1029/jz069i024p05181, 1964.

Roach, L. A., Horvat, C., Dean, S. M., and Bitz, C. M.: An Emergent Sea Ice Floe Size Distribution in a Global Coupled Ocean-Sea Ice Model, Journal of Geophysical Research: Oceans, 123, 4322–4337, https://doi.org/10.1029/2017jc013692, 2018.

Roach, L. A., Bitz, C. M., Horvat, C., and Dean, S. M.: Advances in Modeling Interactions Between Sea Ice and Ocean Surface Waves, Journal of Advances in Modeling Earth Systems, 11, 4167–4181, https://doi.org/10.1029/2019ms001836, 2019.

Robinson, N. and Palmer, S.: A modal analysis of a rectangular plate floating on an incompressible liquid, Journal of Sound and Vibration, 142, 453–460, https://doi.org/10.1016/0022-460x(90)90661-i, 1990.

Rothrock, D. A. and Thorndike, A. S.: Measuring the sea ice floe size distribution, Journal of Geophysical Research, 89, 6477, https://doi.org/10.1029/jc089ic04p06477, 1984.

Squire, V. A.: Ocean Wave Interactions with Sea Ice: A Reappraisal, Annual Review of Fluid Mechanics, 52, 37–60, https://doi.org/10.1146/annurev-fluid-010719-060301, 2020.

Squire, V. A. and Moore, S. C.: Direct measurement of the attenuation of ocean waves by pack ice, Nature, 283, 365–368, https://doi.org/10.1038/283365a0, 1980.

Steele, M.: Sea ice melting and floe geometry in a simple ice-ocean model, Journal of Geophysical Research: Oceans, 97, 17 729–17 738, https://doi.org/10.1029/92jc01755, 1992.

Steer, A., Worby, A., and Heil, P.: Observed changes in sea-ice floe size distribution during early summer in the western Weddell Sea, Deep Sea Research Part II: Topical Studies in Oceanography, 55, 933–942, https://doi.org/10.1016/j.dsr2.2007.12.016, 2008.

Stern, H. L., Schweiger, A. J., Zhang, J., and Steele, M.: On reconciling disparate studies of the sea-ice floe size distribution, Elementa: Science of the Anthropocene, 6, https://doi.org/10.1525/elementa.304, 2018.

Stroeve, J., Holland, M. M., Meier, W., Scambos, T., and Serreze, M.: Arctic sea ice decline: Faster than forecast, Geophysical Research Letters, 34, https://doi.org/10.1029/2007gl029703, 2007.

Thomson, J. and Rogers, W. E.: Swell and sea in the emerging Arctic Ocean, Geophysical Research Letters, 41, 3136–3140, https://doi.org/10.1002/2014gl059983, 2014.

Thorndike, A. S., Rothrock, D. A., Maykut, G. A., and Colony, R.: The thickness distribution of sea ice, Journal of Geophysical Research, 80, 4501–4513, https://doi.org/10.1029/jc080i033p04501, 1975.

Toyota, T., Takatsuji, S., and Nakayama, M.: Characteristics of sea ice floe size distribution in the seasonal ice zone, Geophysical Research Letters, 33, https://doi.org/10.1029/2005gl024556, 2006.

Toyota, T., Haas, C., and Tamura, T.: Size distribution and shape properties of relatively small sea-ice floes in the Antarctic marginal ice zone in late winter, Deep Sea Research Part II: Topical Studies in Oceanography, 58, 1182–1193, https://doi.org/10.1016/j.dsr2.2010.10.034, 2011.

Virtanen, P., Gommers, R., Oliphant, T. E., Haberland, M., Reddy, T., Cournapeau, D., Burovski, E., Peterson, P., Weckesser, W., Bright, J., van der Walt, S. J., Brett, M., Wilson, J., Millman, K. J., Mayorov, N., Nelson, A. R. J., Jones, E., Kern, R., Larson, E., Carey, C. J., Polat, İ., Feng, Y., Moore, E. W., VanderPlas, J., Laxalde, D., Perktold, J., Cimrman, R., Henriksen, I., Quintero, E. A., Harris, C. R., Archibald, A. M., Ribeiro, A. H., Pedregosa, F., van Mulbregt, P., and SciPy 1.0 Contributors: SciPy 1.0: Fundamental Algorithms for Scientific Computing in Python, Nature Methods, 17, 261–272, https://doi.org/10.1038/s41592-019-0686-2, 2020.

Wadhams, P., Squire, V. A., Goodman, D. J., Cowan, A. M., and Moore, S. C.: The attenuation rates of ocean waves in the marginal ice zone, Journal of Geophysical Research, 93, 6799, https://doi.org/10.1029/jc093ic06p06799, 1988.

Wang, Y., Holt, B., Rogers, W. E., Thomson, J., and Shen, H. H.: Wind and wave influences on sea ice floe size and leads in the Beaufort and Chukchi Seas during the summer-fall transition 2014, Journal of Geophysical Research: Oceans, 121, 1502–1525, https://doi.org/10.1002/2015jc011349, 2016.

Williams, T. and Porter, R.: The effect of submergence on the scattering by the interface between two semi-infinite sheets, Journal of Fluids and Structures, 25, 777–793, https://doi.org/10.1016/j.jfluidstructs.2009.02.001, 2009.

Williams, T. D., Bennetts, L. G., Squire, V. A., Dumont, D., and Bertino, L.: Wave–ice interactions in the marginal ice zone. Part 1: Theoretical foundations, Ocean Modelling, 71, 81–91, https://doi.org/10.1016/j.ocemod.2013.05.010, 2013.

Williams, T. D., Rampal, P., and Bouillon, S.: Wave-ice interactions in the neXtSIM sea-ice model, The Cryosphere Discussions, pp. 1–28, https://doi.org/10.5194/tc-2017-24, 2017.

Williams, T. D. C.: Reflections on ice : scattering of flexural gravity waves by irregularities in Arctic and Antarctic ice sheets, Ph.D. thesis, University of Otago, 2006.

Zhang, J., Schweiger, A., Steele, M., and Stern, H.: Sea ice floe size distribution in the marginal ice zone: Theory and numerical experiments, Journal of Geophysical Research: Oceans, 120, 3484–3498, https://doi.org/10.1002/2015jc010770, 2015.

Zhang, J., Stern, H., Hwang, B., Schweiger, A., Steele, M., Stark, M., and Graber, H. C.: Modeling the seasonal evolution of the Arctic sea ice floe size distribution, Elementa: Science of the Anthropocene, 4, https://doi.org/10.12952/journal.elementa.000126, 2016.

Zhang, L., Delworth, T. L., Cooke, W., and Yang, X.: Natural variability of Southern Ocean convection as a driver of observed climate trends, Nature Climate Change, 9, 59–65, https://doi.org/10.1038/s41558-018-0350-3, 2018.